JGR Space Physics

RESEARCH ARTICLE
10.1029/2021JA029716

Key Points:

- Modeling shows that discrete aurora occurs more likely on small-scale patches embedded inside strong crustal field regions
- Auroral occurrence probability greatly increases during space weather events, particularly in weak crustal field regions
- Discrete aurora is not caused by the direct entry of magnetosheath plasma but due to the recycling of nightside magnetospheric electrons

Supporting Information:

Supporting Information may be found in the online version of this article.

Correspondence to:

X. Fang,
Xiaohua.Fang@lasp.colorado.edu

Citation:

Fang, X., Ma, Y., Schneider, N., Girazian, Z., Luhmann, J., Milby, Z., et al. (2022). Discrete aurora on the nightside of Mars: Occurrence location and probability. *Journal of Geophysical Research: Space Physics*, *127*, e2021JA029716. https://doi.org/10.1029/2021JA029716

Received 29 JUN 2021
Accepted 5 FEB 2022

Discrete Aurora on the Nightside of Mars: Occurrence Location and Probability

Xiaohua Fang[1], Yingjuan Ma[2], Nick Schneider[1], Zach Girazian[3], Janet Luhmann[4], Zachariah Milby[1], Sonal Jain[1], Yaxue Dong[1], Shannon Curry[4], and Bruce Jakosky[1]

[1]Laboratory for Atmospheric and Space Physics, University of Colorado, Boulder, CO, USA, [2]Department of Earth, Planetary and Space Sciences, University of California, Los Angeles, CA, USA, [3]Department of Physics and Astronomy, University of Iowa, Iowa City, IA, USA, [4]Space Sciences Laboratory, University of California, Berkeley, CA, USA

Abstract This paper represents the first attempt to predict the occurrence location and probability of discrete electron aurora on the nightside of Mars. We run a 3-D time-dependent magnetohydrodynamic model to characterize the spatial and temporal dynamics of magnetic field and plasma distributions over the course of one planetary rotation. We perform eight simulation cases under solar minimum quiet-solar-wind conditions (four equinox/solstice seasons, each with two interplanetary magnetic field polarities) and in an actual interplanetary coronal mass ejection (ICME) case to assess quiet and space weather situations, respectively. The occurrence of detectable discrete aurora is subject to the combination of the probabilities that (a) the ionosphere is magnetically connected with high altitudes through open field lines and (b) precipitating energy fluxes of >30 eV electrons exceed 0.1 erg/cm^2/s. Our results show that during quiet solar activity, discrete aurora occurs likely on small-scale patches embedded inside strong crustal magnetic field regions (with a magnitude greater than 50 nT at 150 km), and the overall chance across the globe is ~0.77%. The higher probability over strong crustal field regions is attributed to the stronger magnetic field convergence. Modeling shows the occurrence probability dramatically increases during the ICME event, particularly by more than an order of magnitude in weak crustal field regions. Our model results reasonably agree with NASA Mars Atmosphere and Volatile EvolutioN and Mars Express observations. Our study suggests that nightside discrete electron aurora is not caused by the direct entry of magnetosheath plasma in a cusp-like process but due to the recycling of nightside magnetospheric electrons.

Plain Language Summary This paper represents the first attempt to predict the occurrence location and probability of discrete electron aurora at Mars on a planetary scale. Discrete aurora is a patchy and sporadic phenomenon, posing a daunting challenge for understanding how and where auroral electron precipitation takes place in the ionosphere. To address this challenge, we apply a state-of-the-art global model to characterize the spatial and temporal dynamics of near-Mars plasma and magnetic field environments. We simulate the penetration of energetic electrons from high altitudes to the nightside ionosphere through open magnetic field lines, a process responsible for auroral emissions. Our results show that during quiet solar activity, the overall chance of observing a discrete auroral event on the nightside is only ~0.77% across the globe, but the odds are significantly higher over strong crustal field regions. The occurrence probability is enhanced globally during an extreme space weather event, especially in weak crustal field regions. This study reveals a different source mechanism from the prevailing hypothesis that discrete aurora may be excited by the direct entry of magnetosheath plasma in a cusp-like process. Instead, we propose that it is caused by the recycling of nightside magnetospheric electrons that return to the ionosphere.

1. Introduction

Aurorae are light emissions excited through collisional interaction between energetic charged particles and atmospheric constituents. While today's Mars has no intrinsic dipole magnetic field, the presence of locally concentrated and globally scattered crustal magnetic anomalies (Acuna et al., 1998) has prompted theoretical speculation that the Martian atmosphere should also be brightened by auroral activities. So far, three types of aurora have been observationally discovered: discrete aurora (e.g., Bertaux et al., 2005), diffuse aurora (e.g., Schneider et al., 2015), and proton aurora (e.g., Deighan et al., 2018).

The latter two forms of the aurora are geographically widespread, in association with the large-scale interaction between the Mars atmosphere and external drivers. Diffuse electron aurora occurred with similar timing as solar energetic particle (SEP) events and was estimated to be near an altitude of 60–70 km in response to the impact of ∼100 keV SEP electrons (Schneider et al., 2015, 2018). As SEPs originate from an acceleration region with a large spatial scale either at Sun or in interplanetary space, the SEP-induced diffuse aurora on weakly magnetized Mars is global in nature. Proton aurora is another large-scale phenomenon in association with enhanced hydrogen Lyman-α emission, mainly occurring on the dayside of Mars (Deighan et al., 2018). Proton aurora is caused by penetrating energetic neutral atoms, which are converted from solar wind protons through charge exchange with the planetary hydrogen corona beyond the bow shock. Proton aurora peaks near 130 km altitude, which is consistent with the solar wind proton energy of the order of keV.

In contrast with diffuse electron aurora and proton aurora, discrete electron aurora is a geographically-confined and sporadic phenomenon at Mars. All of the discrete auroral events detected by the European Space Agency's Mars Express (MEX) ultraviolet observations were located over strong crustal field regions in the southern hemisphere (Bertaux et al., 2005; Gérard et al., 2015; Leblanc et al., 2008; Soret et al., 2016). Rather than being uniformly spread throughout the region with a strong crustal field, auroral emission was detected in small-scale patches, which coincide with where the statistical probability of having closed magnetic field lines is minimal (Brain et al., 2007). These observations point to discrete aurora as a sporadic and stochastic process. Auroral detections are often found to be unrepeatable over the course of preceding or following orbits to a successful detection orbit, even though geographic coverage is similar and no apparent external factors are causing orbital differences in auroral occurrence. Multiple auroral events sometimes were captured during a single MEX periapsis passage, which was separated in time by a few seconds to tens of seconds and showed no noticeable connection with one another. It is worth noting that discrete auroral observations have been limited to night time to avoid interference from non-auroral processes on the dayside.

Discrete auroral signatures have been extensively searched in ultraviolet observations obtained from the MEX instrument of Spectroscopy for the Investigation of the Characteristics of the Atmosphere of Mars (SPICAM) in nadir and limb viewing geometries. Soret et al. (2016) reported that auroral emissions from the CO Cameron bands (190–270 nm) were peaked near ∼130 km altitude. Auroral events were usually accompanied by a nearly concurrent electron flux enhancement in measurements of the Analyzer of Space Plasma and Energetic Atoms on board MEX. Auroral electrons were estimated to have energy from tens of eV up to ∼300 eV (Leblanc et al., 2008). There is a reasonably high correlation in occurrence site and timing among auroral emissions, energetic electron precipitation, and dominance of open magnetic field topology. However, what is puzzling, and so far unresolved, is the lack of apparent correlation between auroral brightness and precipitating electron fluxes in MEX data. Part of the difficulty in performing such an analysis is that the electrons presumably responsible for the aurora are observed on orbiting spacecraft high above the ionosphere, while the magnetic field lines between the obiter and the ionosphere—along which the precipitating electrons travel—can have a complicated path.

More recently, the Imaging UltraViolet Spectrograph (IUVS) instrument onboard the NASA Mars Atmosphere and Volatile EvolutioN (MAVEN) spacecraft has greatly expanded the number of detected discrete auroral events, allowing a statistical analysis of their locations, occurrence probabilities, and controlling factors. The very recent study of Schneider et al. (2021) reports 278 discrete auroral events out of IUVS limb scans. The planet-wide occurrence rate is estimated to be about 1%, with significant enhancement in regions of strong crustal fields. It is found that events occurred preferentially in evening hours and with negative interplanetary magnetic field (IMF) clock angles. Under these favorable conditions, Schneider et al. (2021) suggest that discrete aurora is likely to recur regularly near the strongest magnetic fields.

The source mechanism of discrete aurora has not yet been determined, largely due to its transient nature. One speculation is that photoelectrons in the conjugate dayside ionosphere move along terminator-straddling magnetic field lines and impact the nightside atmosphere (Dubinin et al., 2008; Winningham et al., 2005). However, Liemohn et al. (2007) analyzed the magnetic field topology distributions near the auroral event reported by Bertaux et al. (2005) and found that the magnetic field lines were probably open instead of closed. It was suggested that photoelectron precipitation was unlikely responsible for the specific event, although its general importance is not ruled out. The prevailing view at present is that energetic electrons ultimately of the solar wind origin penetrate along open magnetic field lines deep into the nightside atmosphere, in a process analogous to the direct entry of solar wind electrons in the Earth's cusp regions. A supporting study came from the analysis

of Mars Global Surveyor (MGS) data by Mitchell et al. (2001), in which electron flux spikes were reported to have a magnetosheath-like energy spectrum in the presence of a strong crustal magnetic field radial component. The sites of spikes were located between two adjacent regions of nightside plasma voids (where electron fluxes abruptly dropped by up to three orders of magnitude at all energies). These observations were woven into a hypothetical picture that between two adjacent closed-field-line-dominated plasma voids, highly radial magnetic field lines are present and extend into high altitudes, constituting a cusp-like structure to facilitate the solar wind entry and cause auroral excitation in the atmosphere.

Till now, a systematic picture of where and under what conditions discrete aurora occurs has been lacking. Little is known about whether the occurrence of aurora is determined by the magnetospheric and ionospheric configurations or whether external triggers, such as solar activity, are required. In this study, we make the first attempt to predict the planetary distribution of discrete electron aurora occurrence location and probability on the nightside of Mars and compare our numerical findings with satellite observations. In particular, we use the magnetic topology in a realistic model of the Mars-solar wind interaction, together with assumptions about the electron source, to explore why discrete aurora is detected over limited regions exhibiting a seemingly random behavior.

2. Model and Data

2.1. Global Time-Dependent, Multispecies MHD Model

The 3-D multispecies, single-fluid magnetohydrodynamic (MHD) model of Ma et al. (2014) is applied to self-consistently solve the solar wind and planetary plasma and magnetic field distributions in the near-Mars space. The model runs in the classic Mars-centered Solar Orbital (MSO) coordinate system within the domain of $-24R_M \leq X \leq 8R_M$, $-16R_M \leq Y, Z \leq 16R_M$ (R_M = 3,396 km for one Martian radius). The X axis points toward the Sun, Y is opposite to Mars' solar orbital velocity, and Z completes the right-handed system. The inner model boundary is set to be 100 km above the surface, well below the main ionospheric layer. The model solves mass densities of protons (of both solar wind and planetary origins) and major ionospheric ion species (O_2^+, O^+, CO_2^+), and plasma velocities and temperatures. In MHD calculations, ions and electrons are assumed to have the same velocity and temperature (sharing half of the plasma thermal pressure). The magnetic field consists of two elements: (a) planetary crustal magnetic field, which is specified using the model of Morschhauser et al. (2014) and (b) a spatially-dependent, temporally-evolving induced magnetic field that results from Mars' interaction with the magnetized solar wind. The magnetic field is computed from the magnetic induction equation and is self-consistent with the plasma solutions.

As illustrated by Ma et al. (2014) and Fang et al. (2015); Fang et al. (2017, 2018), the plasma and magnetic field environments at Mars are not static even under quiescent solar conditions, but dynamically evolve with the planetary rotation. This is because as its orientation to the Sun changes, the crustal field continuously changes its distribution in MSO and thus its interaction with the impinging solar wind. The resulting change in the magnetosphere-ionosphere system requires special attention, given the critical role of the global magnetic field configuration in discrete electron auroral onset. Therefore, we carry out time-marching MHD simulations to allow the dynamics of the system to naturally evolve over the entire period of planetary rotation, providing insights not possible under steady-state approximations. For the purposes of the present study, with one exception (described below), we focus on constant external conditions (both solar wind plasma parameters and IMF strength and orientation) for which only planetary rotation and Mars obliquity (season)-related changes are considered. Our time-dependent MHD model has been validated by successfully reproducing along-orbit observations under quiet solar wind conditions by MGS (Ma et al., 2014) and by MAVEN (Ma et al., 2015), and also during interplanetary coronal mass ejection (ICME) events by MAVEN (Ma et al., 2017, 2018).

Magnetic field lines are extracted using the standard fourth-order Runge-Kutta algorithm within the MHD-calculated 3-D magnetic field distributions, which are a combination of the crustal and induced fields. Field line tracing is performed within a domain extending from 100 km altitude up to a radial distance of 5 R_M from the center of the planet. A field line that has both of its ends at the 5-R_M outer boundary is classified as draped (with both ends connected to the solar wind). A field line reaching from 100 km to the 5-R_M surface is regarded as open. For a field line intersecting the altitude of 100 km (at either one end or both ends), we further determine in which hemisphere (dayside or nightside) its footpoint is located. Magnetic field topologies are divided into six categories: (a) draped field lines with both ends connected to the solar wind, (b) open field lines with one end connected

with the dayside ionosphere and the other end is open, (c) open field lines with the ionosphere-connected end on the nightside, (d) closed field lines with both ends in the dayside ionosphere, (e) closed field lines with both ends connected to the nightside ionosphere, and (f) closed field lines straddling the terminator with one end on the dayside and the other end on the nightside.

2.2. Numerical Simulation Cases

Figure 1 shows the global distribution of the intrinsic crustal magnetic field at 150 km altitude in MSO, at representative time points within a planetary rotation period and during representative equinox and solstice seasons in a Mars year. These distributions are viewed in the tail toward the Sun. See the Supporting Information (SI, Figure S1) for an opposite view from the Sun. Although the crustal field distribution is fixed in the geographic coordinate system, its distribution in MSO is always changing with two characteristic time scales. One is from planetary rotation with a period of ∼24.7 hr. The other is due to the seasonal variation of the orientation of the planet's rotation axis with respect to the Sun. Therefore, we perform MHD calculations for the four representative seasons (solar longitude $L_s = 0°, 90°, 180°, 270°$), during each of which the model covers the full rotation period in a time-dependent mode. It is particularly worth noting that the two equinoxes ($L_s = 0°$ and 180°) are not equivalent from the perspective of the Mars-solar wind interaction, as the planetary orientations and thus crustal field distributions in MSO are distinctly different (Figure 1).

To focus on the inherent dynamics within the Mars system, we run the MHD model under quiet, nominal external conditions. The solar wind density and speed are 4 cm^{-3} and 400 km/s, respectively. The IMF follows the Parker spiral with a magnitude of 3 nT. The IMF is in the ecliptic plane and has a cone angle of 56° (which is the angle between the IMF direction and the Sun-Mars line). To quantify the sensitivity of the downstream magnetic field configuration to the IMF direction, we test two IMF conditions: $(B_X, B_Y, B_Z) = (1.634, -2.516, 0)$ nT and $(-1.634, 2.516, 0)$ nT, representing the nominal toward and away sectors or polarities. Altogether, a total of eight time-dependent MHD cases (four seasons by two IMF polarities) are simulated under quiet solar wind conditions. To facilitate comparison with MAVEN data that were acquired mostly near solar minimum, the photoionization frequency is set to be appropriate for solar minimum at 1 AU (see table 9.2 of Schunk and Nagy [2009]) and then scaled by the inverse square of the Sun-Mars distance. Note that this distance is seasonally dependent (1.56/1.66/1.47/1.39 AU at $Ls = 0°/90°/180°/270°$, respectively), and so is the solar EUV flux reaching the planet. Fixing the EUV flux at Sun rather than at Mars allows us to characterize the realistic responses of the Martian system at comparable solar activities. It takes ∼30,000 CPU hr to complete one time-dependent MHD run on supercomputers. The model results are output at a time cadence of 20 min for analysis.

Besides the quiet solar wind cases, we add to our analysis an ICME case during 13 September 2017 ($L_s \approx 60°$). This event is one of the most powerful space weather events that have been observed at Mars, whose time-evolving impact on the Mars magnetosphere-ionosphere system has been analyzed using the MHD model and validated by the close agreement with MAVEN measurements (Ma et al., 2018). The simulated time interval is from September 12, 22:00 UT (∼5 hr prior to the ICME shock arrival) to September 13, 10:55 UT, and the results are exported at a fine time cadence of 5 min for analysis. Despite that the specific ICME simulation does not cover a full planetary rotation period, the comparison between quiet and disturbed solar wind conditions provides an insight into the impact of space weather events.

2.3. MAVEN IUVS Discrete Auroral Observations

Numerical simulation results will be tested by comparing with MAVEN IUVS ultraviolet observations. IUVS discrete auroral detections and non-detections on the nightside have been reported by Schneider et al. (2021), which are accessible through the Findable, Accessible, Interoperable, and Reusable data repository listed in that paper. The details on IUVS limb scan observations and auroral detection methodology have been included in Schneider et al. (2021), and thus are not repeated here. The currently available IUVS auroral observations cover the time period of 1 December 2014 (orbit 335) to 7 May 2020 (orbit 11,484). For this work, we omit auroral events with apparent altitudes below 100 km, where the emission has been determined to arise from patches in the foreground or background. The positional accuracy of localized emission patches is best when the emission lies at the limb but is reduced when the emission patch lies in the foreground or background. Therefore, low-apparent-altitude cases (below 100 km) are excluded, considering that uncertainty in the location along the line of

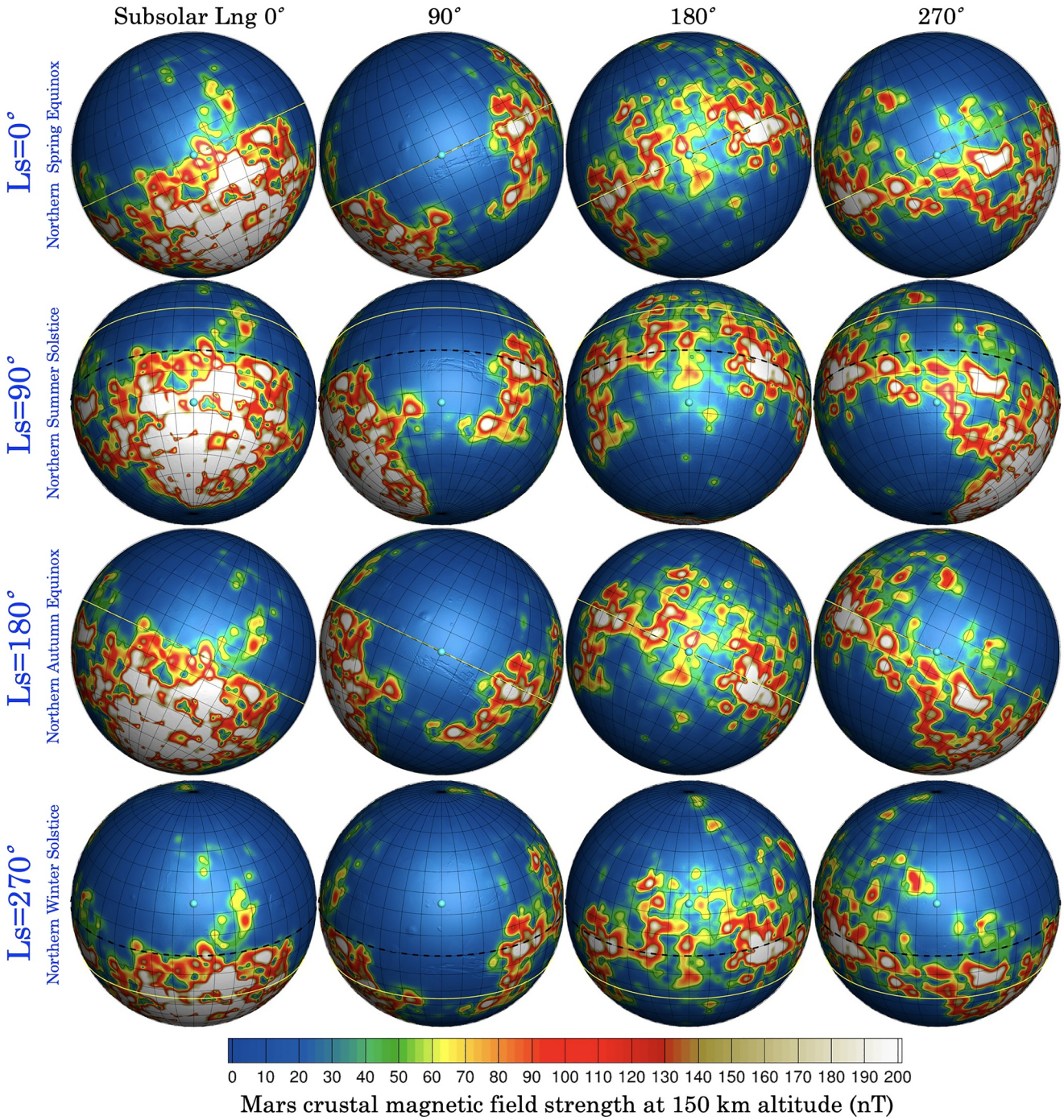

Figure 1. Distribution of the Mars crustal magnetic field at 150 km altitude calculated using the model of Morschhauser et al. (2014), viewed in Mars centered Solar Orbital (MSO) from the tail toward the Sun (i.e., along the MSO + X direction). The rows from top to bottom present the results during four representative seasons: solar longitude $L_s = 0°$ (northern spring equinox), $L_s = 90°$ (summer solstice), $L_s = 180°$ (autumn equinox), $L_s = 270°$ (winter solstice). Each row shows the temporal variation of the distributions during a planetary rotation period. The panels from left to right are at four representative time points when the subsolar longitude is 0°/90°/180°/270°, which correspond to the strongest crustal field region located at midnight/dusk/noon/dawn, respectively. The crustal field distribution is superposed on the Mars Global Surveyor Mars Orbiter Laser Altimeter topographic map (Smith et al., 2001). The black dashed curve indicates the equatorial circle. The yellow curve shows the latitudinal circle, along which the subsolar point sweeps during planetary rotation. The cyan dot in the panel center indicates the position of the antisolar point.

sight prevents an accurate determination of location relative to the crustal fields. It bears noting that the retained IUVS auroral observations still have an uncertainty of several degrees along the line of sight.

3. Model Results

3.1. A Case Study for $L_s = 0°$, IMF $B_Y < 0$

3.1.1. Magnetic Field Topology

We start with the analysis of one of the quiet solar wind cases, which is during the northern spring equinox ($L_s = 0°$) and corresponds to a toward IMF sector polarity ($B_Y < 0$). We first examine magnetic field topology, which is critical for understanding discrete aurora occurrence. As demonstrated by example magnetic field lines in the SI (Figure S2) for this specific MHD case, the magnetic field configuration is complex in spatial distribution and dynamic in time (cf., e.g., Brain et al., 2007, 2020; Fang et al., 2018; Xu et al., 2017, 2020). The snapshots of magnetic field topology are included in Figure 2. It is seen that closed field lines predominate at 150 km altitude, on both dayside and nightside. A close look at the strong crustal field region near 50°S latitude reveals the presence of very narrow patches in the ionosphere, over which field lines tend to have an open topology (white and red shading indicating dayside and nightside magnetic connections, respectively). These open-field-line regions are surrounded by predominantly closed-field-line regions. The presence of these small-scale open-topology patches is persistent, even though they vary in size over time with planetary rotation and switch intermittently between open and closed field topologies.

Unlike the predominance of closed field lines globally at 150 km altitude, the middle column of Figure 2 shows that at 400 km, open field lines start to dominate the region of weak crustal fields in the northern hemisphere. Throughout this study, we artificially choose the crustal magnetic field magnitude of 50 nT at 150 km as the threshold strength to distinguish between strong and weak crustal field regions, which occupy approximately 28% and 72% of the global area, respectively. It will be shown later that such a choice works reasonably well. In addition, draped field lines (blue shading) start to appear at 400 km but almost exclusively on the dayside. At altitudes as high as 5,000 km, the draped topology is dominant everywhere, except in the central wake of Mars. Within the central tail of SZA > 135°, nightside-connected open field lines (red) are near the Sun-Mars line, surrounded by open lines with a dayside connection (white).

The time-dependent MHD simulations enable us to derive the statistical occurrence frequency of different magnetic field topologies over the course of planetary rotation, which is shown in Figure 3. In keeping with the goals of this study, we focus on the nightside. For any longitude-latitude location, we use only those time points when it lies tailward of the terminator (SZA > 90°) and omits the other time points when it faces the Sun. The probability in Figure 3 is calculated as the percentage out of all nightside time points when the topology falls into each of the six categories. It is readily seen that closed magnetic field lines are dominant over strong crustal field regions, nearly all having only nightside footpoints. This dominance extends from the ionosphere up to at least 800 km altitude in the magnetosphere. The terminator-straddling closed field lines are concentrated over polar regions, sometimes extending into weak crustal field regions at middle and low latitudes. Closed field loops with both footpoints on the dayside are occasionally stretched across the terminator into the nightside. On the other hand, the open field topologies dominate weak crustal field regions below 800 km altitude and also show up as dispersed, small-scale patches in the region of strong crustal fields. It is worth noting that the patches embedded inside strong crustal field regions are those where the discrete aurora is observed relatively more frequently (Schneider et al., 2021). At high latitudes near the poles, particularly above 400 km altitude, field lines are more likely open with their footpoints located on the dayside than on the nightside. At altitudes above 800 km, the occurrence of draped field lines increases and dominates.

3.1.2. Electron Precipitation

The prevailing hypothesis on discrete auroral generation is that open magnetic field lines constitute an effective channel for energetic electrons at high altitudes to penetrate into and excite the upper atmosphere. In this section, we follow this scenario to quantify the global distribution of precipitating electron energy fluxes. Magnetic field lines are extracted on a fine, regular spherical grid at a high altitude of 5,000 km. Wherever an open field line is formed, the local MHD plasma is able to move downward and strike the upper atmosphere at the field line

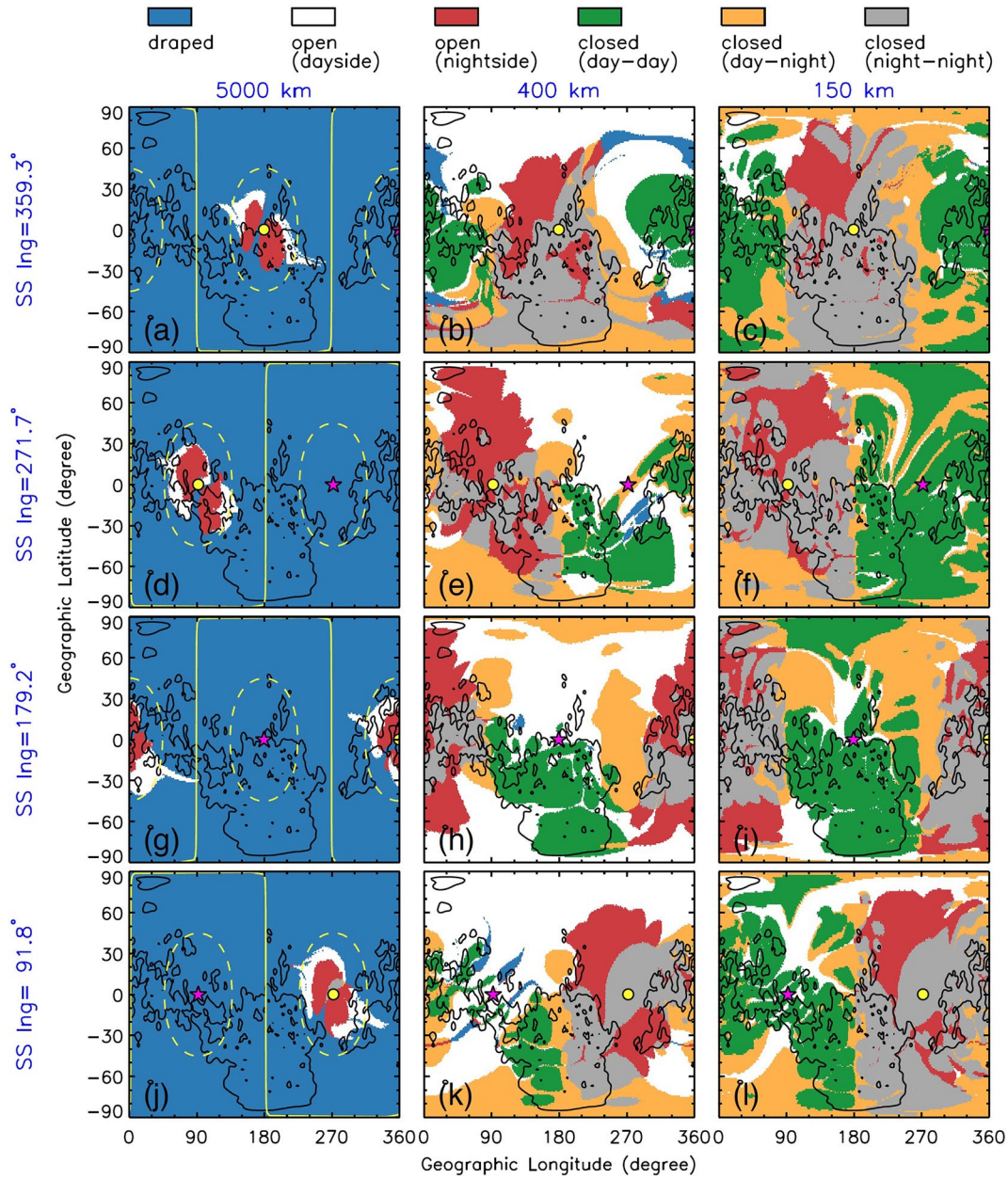

Figure 2. Global distribution of magnetic field topology in the quiet solar wind magnetohydrodynamics case of $L_s = 0°$, interplanetary magnetic field $B_Y < 0$. Different colors indicate different types of topologies as noted in the legend at top of panels. The rows from top to bottom show the results at four representative time points during the planetary rotation when the subsolar longitude varies (as marked to the left of the panels). The columns from left to right show the results at 5,000 km, 400 km, and 150 km altitude, respectively. In each panel, the contour line of crustal magnetic field strength of 50 nT at 150 km altitude is superposed for reference to strong crustal field regions, using the model of Morschhauser et al. (2014). The magenta star and yellow dot mark the positions of subsolar and antisolar points, respectively. In the left-most column, the projection of the terminator (with a solar zenith angle, SZA, of 90°) is overplotted in a solid yellow curve, and the positions of SZA = 45° and 135° are marked in yellow dashed curves.

footpoint. Here we take advantage of an important feature of our approach that magnetic field and plasma distributions are globally and self-consistently solved in the model.

Under the MHD fluid-like approximation, precipitating electrons consist of thermal plasma populations with Maxwellian energy distribution. Using the model-calculated electron density and temperature, the energy spectrum of precipitating particles (similar to those reported by Verigin et al. [1991]) can be estimated from the

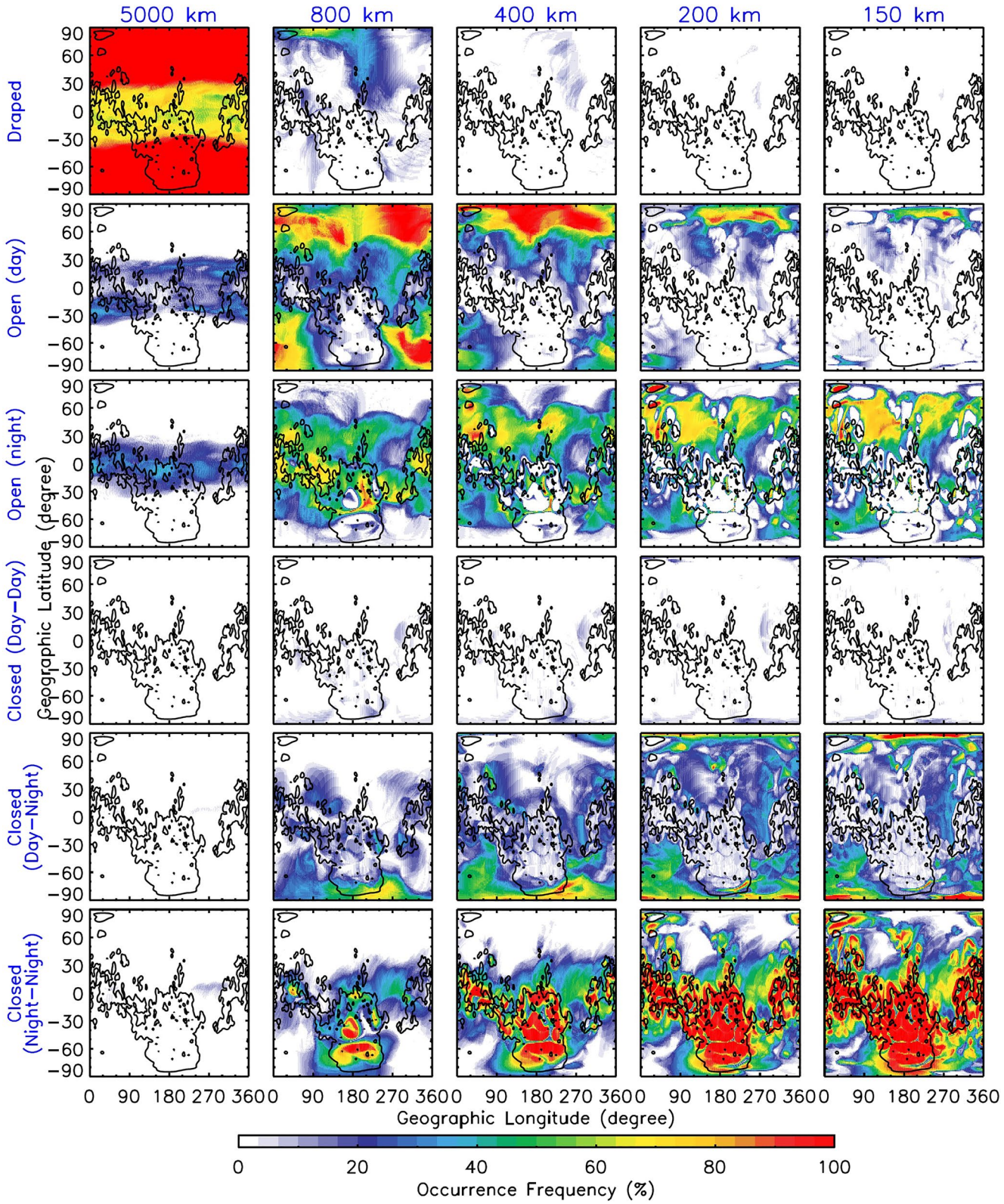

Figure 3. Occurrence probability of magnetic field topology on the nightside (SZA > 90°) in the quiet solar wind magnetohydrodynamic case of $L_s = 0°$, interplanetary magnetic field $B_Y < 0$. From top to bottom, the examined topologies are draped, dayside-connected open, nightside-connected open, closed with both ends on the dayside, terminator-straddling closed, and closed with both ends on the nightside. From left to right, the results are given at various altitudes: 5,000 km, 800 km, 400 km, 200 km, and 150 km. The contour line of crustal field strength of 50 nT at 150 km is superposed for reference.

classic gas dynamics. Given that the kinetic energy considerably overweighs the plasma bulk speed, precipitating electrons are approximately in an isotropic angular distribution, which is consistent with MGS observations (Brain et al., 2007). The differential number flux over the downward traveling hemisphere, under the assumption of a Maxwellian-Boltzmann distribution, is thus written as

$$\phi(E) = (2\pi m)^{-1/2}\, n_e\, (kT_e)^{-3/2}\, E \exp\left(-\frac{E}{kT_e}\right), \tag{1}$$

where k is the Boltzmann constant, m is electron mass, n_e and T_e are the MHD-computed electron number density and temperature at a precipitation source position at 5,000 km altitude. The kT_e term defines the characteristic energy of electrons (at which $\phi(E)$ is peaked), which is half of the average energy. We note that only electrons of sufficiently high energy are able to penetrate to auroral occurrence altitudes before being effectively stopped and absorbed by the exosphere. The Monte Carlo calculation of electron-impact emissions by Soret et al. (2016) suggested that MEX-observed auroral altitudes were consistent with precipitating energies of about 40–200 eV. In this work, we consider magnetospheric electron precipitation in the high energy tail ($E > 30$ eV) of a Maxwellian energy distribution, whose integrated energy flux is given by

$$\begin{aligned} J(E > E_T) &= \int_{E_T}^{\infty} E\, \phi(E)\, dE \\ &= (2\pi m)^{-1/2}\, n_e\, (kT_e)^{3/2} \exp\left(-\frac{E_T}{kT_e}\right)\left(\left(\frac{E_T}{kT_e}\right)^2 + 2\frac{E_T}{kT_e} + 2\right), \end{aligned} \tag{2}$$

where E_T is the threshold energy of 30 eV. It should be pointed out that the resulting column emission rate in the atmosphere is proportional to the incident energy flux, while the peak location and shape of the energy deposition altitude profile depend on the average energy of precipitating particles (see, e.g., Fang, Randall, et al., 2008). Taking this into account, we use the energy flux rather than the number flux as a measure of precipitation intensity.

At any qualifying start point at 5,000 km, where there is an open field line passing through and connected with the nightside ionosphere, we calculate the precipitating energy flux using Equation 2 and multiply it by the area of the spherical bin where the start point is located. We then add the resulting downward energy flow to all the longitude-latitude bins crossed by the field line above 150 km in the ionosphere, as the collisional energy loss at higher altitudes is reasonably negligible. After traversing all the start points, we convert the accumulated energy flows at low altitudes into the energy fluxes by dividing them by the corresponding bin areas. By this means, multiple open field lines originating at 5,000 km altitude may intersect a single bin in the ionosphere. The process of field line tracing and electron precipitation calculation is repeated as we go through each global snapshot of the MHD results that are exported with the planetary rotation. It should be pointed out that the probable acceleration of electrons along their downward penetration paths by magnetic-field-aligned potentials, which has been reported in MEX and MAVEN particle measurements, is not accounted for in our MHD calculations.

Figure 4 (left column) presents the nightside distributions of average precipitating >30 eV electron energy fluxes. At any longitude-latitude location, we estimate how much kinetic energy on average may be brought down from the magnetosphere in the event of electron precipitation, omitting those time points when open field lines are absent. It is seen that intense electron precipitation is mainly concentrated over strong crustal field regions, except in some weak crustal field regions at high latitudes. The precipitation zones are not continuously distributed but spatially spread over the patches where there is a higher chance to expect the open magnetic field topology (Figure 3, third row from the top). In contrast, even though magnetic field lines are more likely open over weak crustal field regions, the average precipitating energy flux therein is considerably smaller, by up to an order of magnitude.

In order to understand the cause of the apparent difference in precipitating energy flux between strong and weak crustal field regions, we examine magnetic field convergence. For a longitude-latitude bin in the ionosphere ("destination"), we first identify all the bins at 5,000 km altitude ("source") where the field lines are open and connected with the same destination bin. The magnetic field convergence factor is then defined as the ratio of the solid angles subtended by all the qualifying source bins and by the destination bin with respect to the planet's center. See Figure S3 in the SI for a schematic diagram of the definition. For idealized radially converging magnetic field lines, the convergence factor would be equal to 1. It is worth noting that here we trace the magnetic

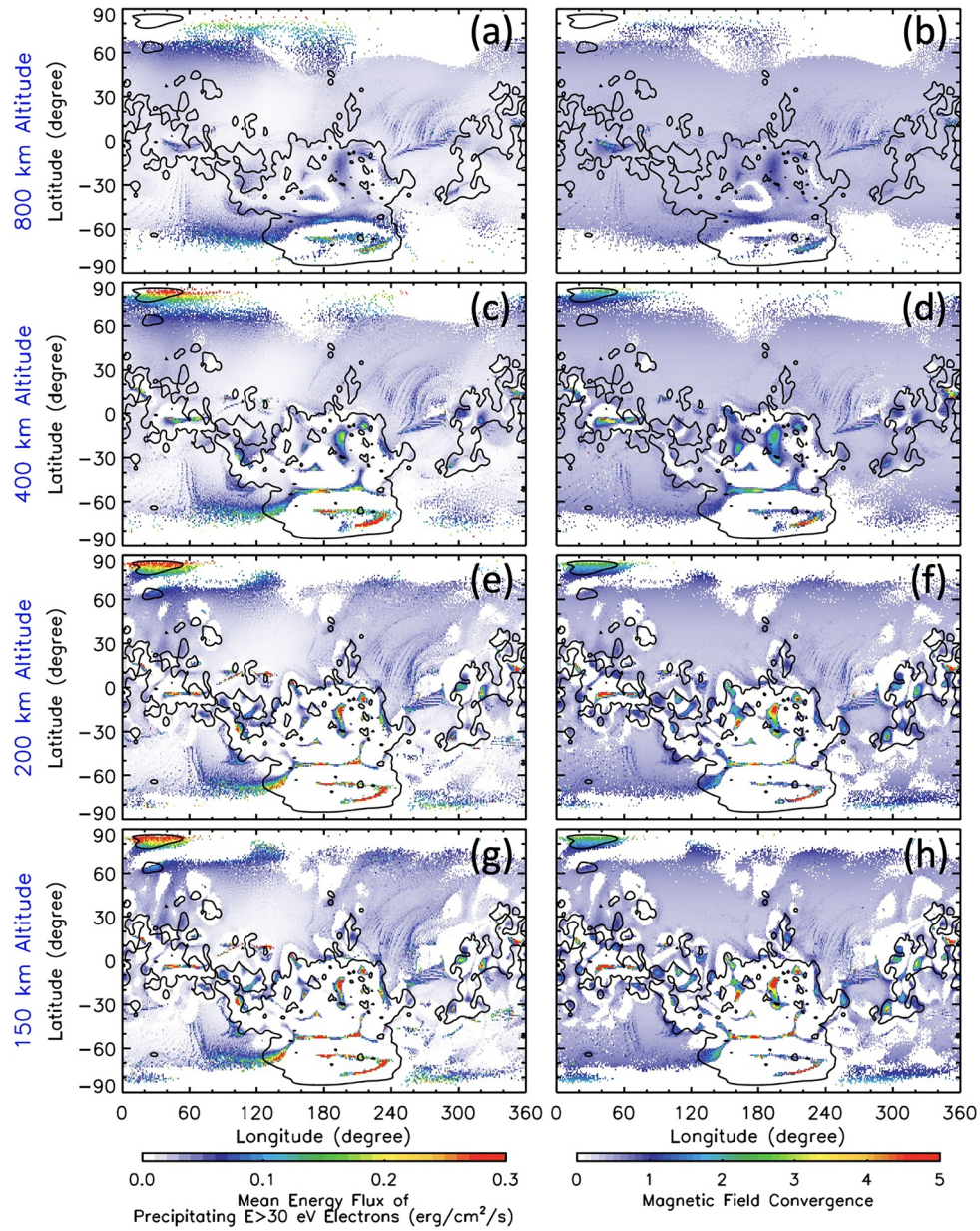

Figure 4. (left) Mean energy flux of precipitating >30 eV electrons on the nightside originating from 5,000 km altitude in the quiet solar wind magnetohydrodynamic case of $L_s = 0°$, interplanetary field $B_Y < 0$. From top to bottom, the results are given at altitudes of 800 km, 400 km, 200 km, and 150 km, respectively. (right) Mean value of magnetic field convergence, which is defined as the ratio of the solid angles spanned by the open magnetic field lines at 5,000 km and at examined altitudes. At any longitude-latitude position, averaging is made over time points when an open field line forms to facilitate magnetospheric electron precipitation. The contour line of crustal field strength of 50 nT at 150 km is superposed for reference.

field line downward from 5,000 km rather than upward from a destination altitude in the ionosphere, similar to the electron precipitation calculation as described above. Although the downward and upward field line tracings are equivalent in theory, they may produce different results due to the limitation of finite longitude-latitude resolutions in numerical calculations. This is because, under the upward field line tracing scheme, a destination bin would be connected to either none (if the passing field line is not open) or a single source bin at high altitudes, as field lines are traced only at bin centers. As a consequence, it is possible that the magnetic connection with some

source bins may have been missed and not evaluated. In this work, we downward trace magnetic field lines to ensure that the field focusing effect is appropriately accounted for.

Figure 4 (right column) shows the convergence factor averaged among the time points when electron precipitation occurs. It is readily seen that the convergence factor is considerably greater than one over strong crustal field regions in the event of electron precipitation, and is near or below one over weak crustal field regions. Due to the dominance of closed field topologies in the ionosphere over strong crustal field regions (Figure 3), open field lines are squeezed into small-scale patches, leading to important convergence. Over strong crustal field regions, the convergence exhibits apparent altitude variation. Starting near 800 km altitude, the magnetic field convergence is significantly enhanced at 400 km, further intensified at 200 km, and then maintained at lower altitudes. In comparison, there is a little variation with altitude in the regions of a weak crustal field. As illustrated by the comparison between the left and right columns of Figure 4, their remarkable consistency, in both the horizontal and altitude variations and over both strong and weak crustal field regions, indicates that the intensification of nightside electron precipitation prominently over strong crustal field regions is attributed to the pronounced increase in magnetic field convergence there.

3.1.3. Discrete Electron Aurora

As discussed above, open field line topology does not necessarily result in an intense energy flux associated with electron precipitation. For an auroral event to be detectable by current technology, significant electron energy fluxes must have been transported from high altitudes to cause ample emissions. We adopt the threshold energy flux of $J_T = 0.1$ erg/cm^2/s at 150 km, which is an artificial but reasonable choice. The MEX-observed auroral electron precipitation reported by Leblanc et al. (2008) has a mean value of ~0.02 erg/cm^2/s (in their Table 2) at high altitudes (~400–950 km). The actual energy fluxes reaching auroral altitudes are expected to be several times higher after the magnetic field convergence is considered according to Figure 4. This gives us confidence that our choice of the threshold energy flux provides a reasonable basis for this work. However, we note that Gérard et al. (2015) estimated higher electron energy fluxes with a peak ranging between 0.1 and 10 erg/cm^2/s.

We follow three steps to quantify the occurrence probability of a detectable auroral event on the nightside over the course of the planetary rotation. First, we calculate the probability (P_1) of precipitation occurrence at a nightside location at 150 km altitude, when an open magnetic field line is connected with a precipitation source region at 5,000 km. The result has been presented in Figure 3 and is reproduced in Figure 5a. Second, we calculate the probability (P_2) of getting an intense precipitating energy flux $J(E > E_T) > J_T$ at 150 km out of all precipitation events during the planetary rotation, whenever the local field lines are open. The spatial distribution of this probability is given in Figure 5b. In accordance with the observation that magnetic field convergence is mainly concentrated over strong crustal field regions, intense precipitation more likely occurs there as well. Third, the occurrence probability of a detectable discrete aurora event is given by $P = P_1 \times P_2$, measuring the combined likelihood that (a) open field lines form to enable downward transport of electrons from high-altitude precipitation source regions and (b) incident fluxes are strong enough for the resulting emissions to be observable. As shown in Figure 5c, the P distribution follows a similar pattern as P_2 (Figure 5b), after the regulation of the magnitude by P_1 (Figure 5a). Note that there is no significant change with altitude below 200 km in the probabilities of both the nightside-connected open field topology (Figure 3) and magnetic field convergence (Figure 4).

Considering that a regular longitude-latitude grid has various bin areas (which are maximal near the equator and minimal at the poles), we derive an overall chance in a broad region by weighing in bin areas as below

$$\langle P_i \rangle = \frac{\iint P_i(\theta, \phi) \cos\theta \, d\theta \, d\varphi}{\iint \cos\theta \, d\theta \, d\varphi}, \tag{3}$$

where φ and θ are longitude and latitude. P_i in the equation can be P_1, P_2, or P as defined above. When integrating over strong crustal field regions (>50 nT at 150 km), we have the odds of 1.49% to get a detectable auroral event in this specific MHD case. This means that for N random nighttime observations ($N \gg 1$) that are uniformly spread within those geographic regions, $0.0149N$ discrete auroral events would be expected on average. Similarly, the overall chances over weak crustal field regions and across the globe are 0.39% and 0.7%, respectively. These area-averaged values for P together with those for P_1 and P_2 are marked in Figure 5. In this case, over strong crustal field regions, although $\langle P_1 \rangle$ is only ~1/3 of that over weak crustal field regions, $\langle P_2 \rangle$ is ~3 times greater, leading to a more than the triple chance of detectable auroral occurrence $\langle P \rangle$.

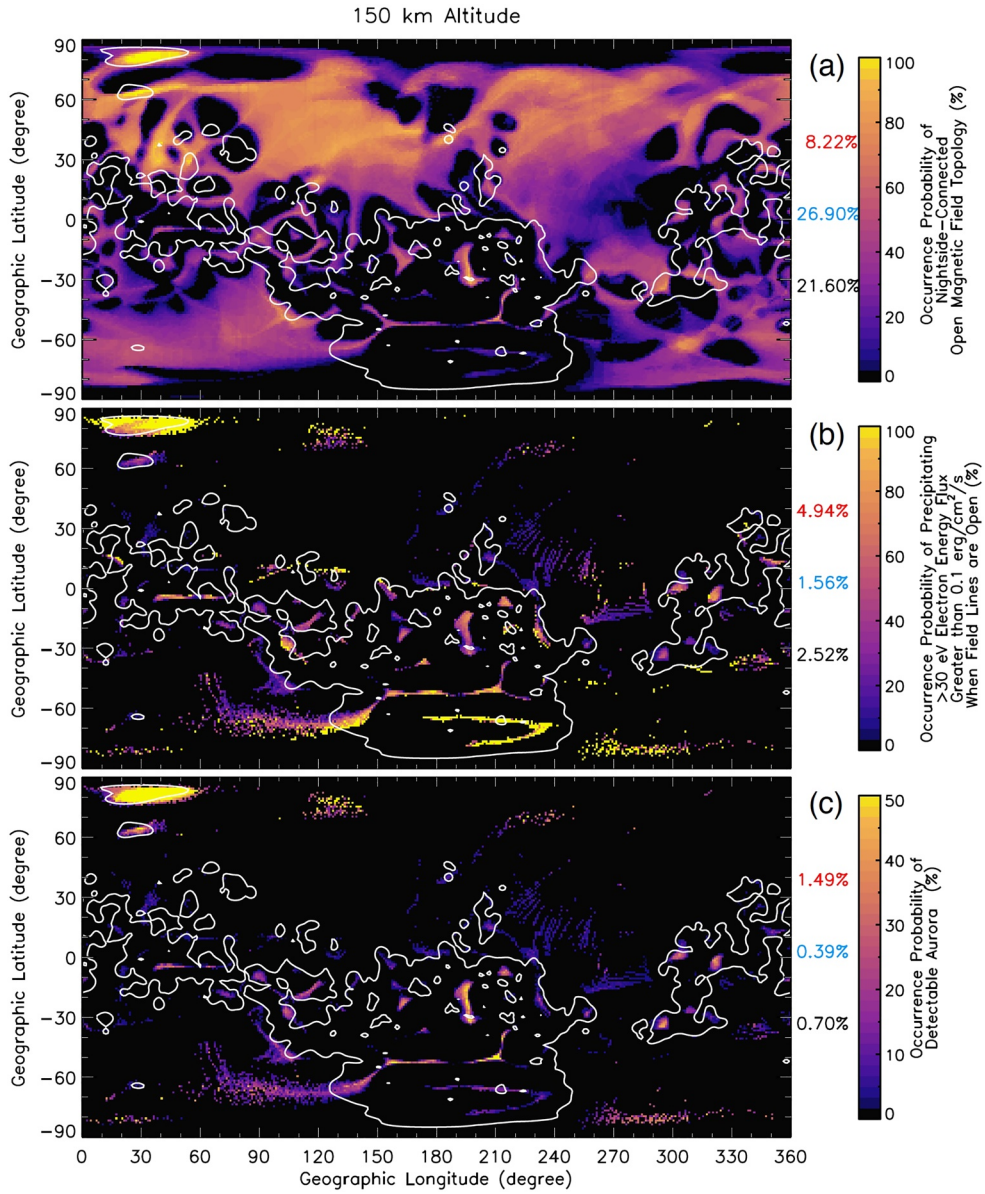

Figure 5. Discrete aurora occurrence location and probability on the nightside in the quiet solar wind magnetohydrodynamic case of $L_s = 0°$, interplanetary magnetic field $B_Y < 0$. Panel (a) shows the occurrence probability of a nightside-connected open magnetic field topology at 150 km altitude, which is replotted from Figure 3. Panel (b) shows the probability of having a more than 0.1 erg/cm^2/s energy flux of precipitating >30 eV electrons at 150 km altitude. Panel (c) presents the discrete aurora occurrence probability, which is obtained by multiplying the above two probabilities. The overall chances over strong and weak crustal field regions as well as globally are calculated and marked on the right side of the panels in red, blue, and black, respectively. Note that the color scale of panel (c) is different from those in panels (a) and (b). The contour line of crustal field strength of 50 nT at 150 km is superposed for reference.

A numerical experiment has been performed to assess the sensitivity of the estimated occurrence probabilities (specifically, P_2 and P) to the choices of the threshold energy and energy flux, if deviating from the current setup of $E_T = 30$ eV and $J_T = 0.1$ erg/cm^2/s, respectively. Note that the occurrence probability of the nightside-connected open field topology (i.e., P_1) is independent of E_T and J_T. In the sensitivity test, we compare the probability distributions resulting from six combined parameter sets, covering three E_T values (30, 40, 50 eV) by two J_T values (0.1 and 0.2 erg/cm^2/s). As naturally expected and confirmed in the SI (Figure S4), a larger E_T value leads to a reduction in the estimated precipitating energy flux $J(E > E_T$; see Equation 2), and the use of a greater J_T value reduces the detection probability of auroral brightness exceeding a threshold level. The fact that the auroral

morphology is fairly stable in the experiment shows that our basic conclusions do not critically depend on the E_T and J_T settings, although they do affect the probability magnitude. As shown in the next section, our choice of $E_T = 30$ eV and $J_T = 0.1$ erg/cm^2/s brings the model predictions close to the MAVEN observations. It is of interest to note that when J_T is doubled in our experiment from 0.1 erg/cm^2/s to 0.2 erg/cm^2/s (equivalent to halving the sensitivity of an ultraviolet instrument), the overall chance of auroral detection would be reduced by more than half. It is implied that the sensitivity difference between MEX and MAVEN ultraviolet instruments needs to be considered in explanation of their dramatically different auroral detection frequencies.

3.2. Comparison Among MHD Cases and With Satellite Ultraviolet Observations

In order to explore the variability of the Martian system under a variety of seasonal and IMF polarity conditions, we extend our discussions from the specific case in Section 3.1 to all the considered representative quiet-solar-wind cases and the ICME case as described in Section 2.

Figure 6 presents the nightside probability distributions of magnetic field topology at 400 km altitude by averaging all the quiet-solar-wind cases. The topologies are grouped into two categories for comparison: open/draped (with at least one end open) and closed (regardless of the hemispheres in which the ionospheric footpoints are located). We calculate the topology probability over the planetary rotation (similar to Figure 3), and then make an arithmetic average among the four seasons under each IMF polarity condition (in the toward/away IMF sectors). The numerical predictions are compared with the MGS results of Brain et al. (2020). The remarkably close agreement provides another validation of our numerical approach.

Statistically speaking, the field lines over strong crustal field regions are dominantly closed (except for dispersed, small-scale patches), and open/draped field lines are predominant over weak crustal field regions. This highlights the strong control of the crustal magnetic field, particularly its magnitude, in the ionosphere. Furthermore, the clear-cut division justifies our use of 50 nT at 150 km as the threshold strength between strong and weak field regions. The general similarity between Figures 3 and Figures 6a–6b indicates that the seasonal dependence is not strong. The sensitivity to the IMF polarity, as examined in Figure 6, is discernible but not distinct. It should be pointed out that the model and data are not compared under identical conditions. The MGS data were collected during many Mars years under the various solar wind, IMF, and solar radiation conditions, and the local time sampling was restricted to its 2a.m.-2p.m. orbits. The magnetic field topology cannot be measured but was inferred with uncertainties from suprathermal electron energy and angular distributions. Therefore, the strikingly close agreement between the model and data implies that the topologies, in binary classification, have relatively stable probability distributions that are not strongly influenced by external conditions. This also supports the representativeness of our cases in the exploration of the average behavior of the Mars magnetic environment.

We extend the calculation of the detectable auroral occurrence probability from the specific case in Figure 5c to all the quiet solar wind cases. As demonstrated in the SI (Figure S5), the intercomparison among the cases shows a consistent spatial distribution, albeit being strengthened or weakened at some regions under certain seasons and IMF polarities. The average distributions are presented in Figure 7a to highlight those prevalent features. Specifically, the best chance to observe discrete aurora during quiet solar activity is at small-scale patches embedded inside strong crustal field regions. Over weak crustal field regions, the aurora may be present near the southern and northern polar regions (poleward of ~75°) during the seasons of $L_s = 90°$ and $L_s = 270°$, respectively. As shown in both the model prediction and the IUVS data, the occurrence probability is also noticeably enhanced over a narrow latitude band west of the strongest crustal field area in the southern hemisphere, roughly between 60°S and 75°S latitudes. On this east-west stretched latitude band, enhanced precipitating suprathermal electron number fluxes have also been observed by MGS (Lillis & Brain, 2013).

The 13 September 2017 ICME case is examined in Figure 7b to evaluate the effects of space weather events. In addition to a significant enhancement in the probability of occurrence over the small-scale patches inside strong crustal field regions, the most prominent feature is the dramatic increase across weak crustal field regions (where the odds of observing aurora are typically low during quiet solar activity). In contrast with a factor of 3 increase in the overall chance over strong crustal field regions (from 1.81% to 5.76%), the increase over weak crustal field regions is more than an order of magnitude reaching a factor of 27 (from 0.35% to 9.39%). Across the globe, there is a factor of 11 increase, from 0.77% to 8.30%. As explained in the SI (Figures S6-S8), these increases are mainly due to a dramatic jump in the probability of precipitating >30 eV energy flux greater than 0.1 erg/cm^2/s

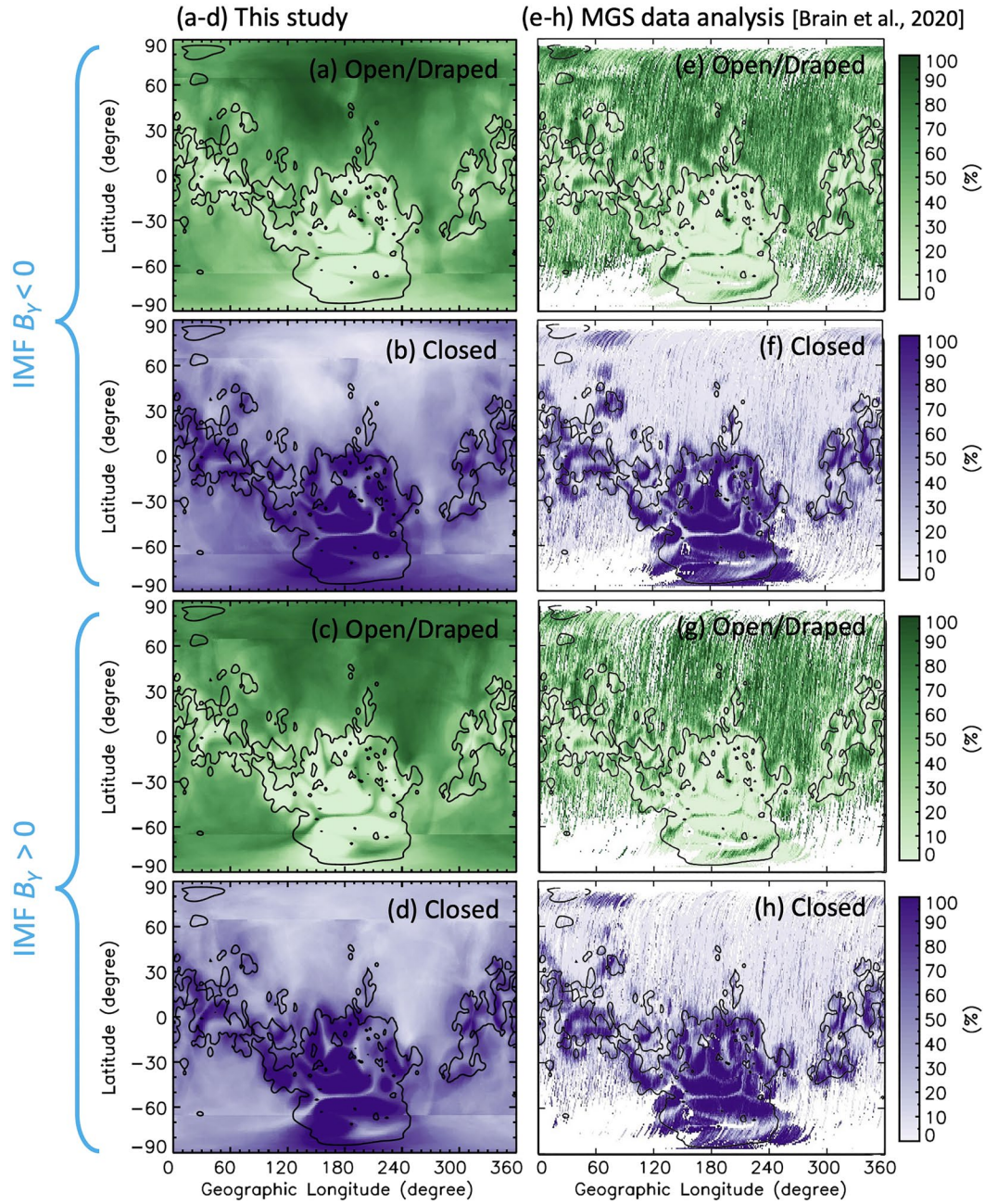

Figure 6. Occurrence probability of open and draped field line topologies (green shading) and closed field line topologies (purple shading) at 400 km altitude on the nightside, when the upstream interplanetary magnetic field is oriented with its Mars centred Solar Orbital component $B_Y < 0$ (in the top two rows) or $B_Y > 0$ (in the bottom two rows), respectively. The left column shows our magnetohydrodynamic simulation results averaged over the four representative seasons, and the right column is adopted from the statistical analysis results using ~7-year Mars global surveyer (MGS) data by Brain et al. (2020). The white shading in the MGS plots, particularly near polar regions, indicates the lack of either data or meaningful statistics. The contour line of crustal field strength of 50 nT at 150 km is superposed for reference.

across the globe, which results from the great enhancement of the magnetotail plasma density and temperature during the ICME event. On the other hand, for the occurrence probability of the nightside-connected open field topology, despite a small increase over strong crustal field regions, there is a significant decrease over weak crustal field regions. The latter is accompanied by an increase of the probability of the dayside-connected magnetic field topology (see Figure S7 in the SI for the occurrence probability of magnetic field topology in the event),

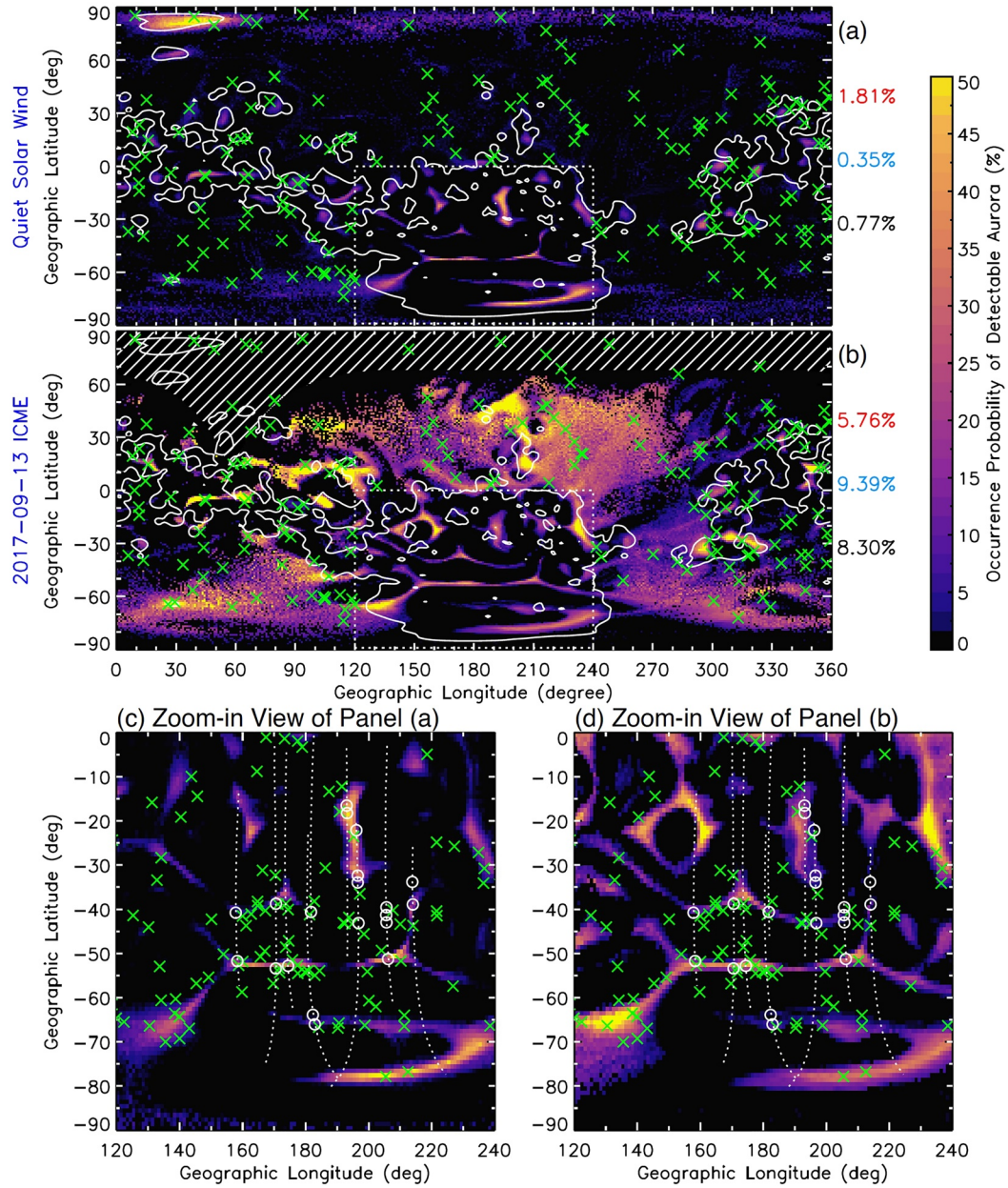

Figure 7. Magnetohydrodynamic-derived discrete auroral occurrence probability on the nightside (a) under quiet solar wind conditions by averaging the eight cases (see the SI), and (b) during the 13 September 2017 interplanetary coronal mass ejection event. The overall chances averaged over strong and weak crustal field regions as well as globally are marked on the right side of the panels in red, blue, and black, respectively. The contour line of crustal field strength of 50 nT at 150 km is superposed for reference. Green '×' symbols mark the longitude-latitude positions of the auroral events observed by Mars Atmosphere and Volatile EvolutioN Imaging UltraViolet Spectrograph (IUVS) limb scans above 100 km altitude for comparison. For clarity, the IUVS-observed auroral sites are not displayed inside the strong crustal field region highlighted by the dashed box. Rather, they are included in panels (c) and (d), which present close-up views of panels (a) and (b), respectively. In the bottom panels, the white dotted lines show the orbital tracks of Mars Express (MEX), along which the detected auroral locations by MEX- Spectroscopy for the Investigation of the Characteristics of the Atmosphere of Mars in its nadir viewing mode are marked with white circles (retrieved from Figure 11 of Gérard et al. [2015]).

which reflects the nightside consequence from the enhanced dayside magnetic reconnection during the disturbed solar activities. Note that this specific ICME event produced one of the most powerful solar wind disturbances at Mars and thus may not be representative of typical space weather events. Nevertheless, it helps assess the limits of the system in an extreme scenario.

Figures 7c and 7d present close-up views of our theoretically predicted auroral occurrence locations inside the main strong crustal field regions, in comparison with ultraviolet observations by MAVEN IUVS (green '×' symbols) and MEX SPICAM (white circles). The IUVS data are adopted from Schneider et al. (2021) and the SPICAM data are retrieved from Gérard et al. (2015). The model-data comparisons show a reasonably good agreement as most of the detected auroral events (especially in nadir-view by MEX) occur where our model predicts a high probability of occurrence, bearing in mind that there is an uncertainty in auroral site estimation in IUVS limb viewing. It is worth noting that a noticeable number of auroral events occurred near the area that spans approximately 35°S – 45°S in latitude and 180°–225° in longitude, despite that the probability is predicted to be low according to Figure 7c. Given that the probability over there is significantly intensified during the ICME event (Figure 7d), we speculate that either these detections happened during space weather events or the upstream IMF direction significantly departed from the Parker spiral in the ecliptic plane that we have assumed in our quiet cases.

Besides the occurrence location, we further compare the occurrence probability by also considering null auroral observations in the data. Figure 8a gives the spatial coverage of MAVEN IUVS auroral observations, which include both detections (as shown in Figure 7) and non-detections. Considering the globally low occurrence probability of less than 1%, we use an ad-hoc irregular grid to ensure at least 100 observations within each longitude-latitude bin so that the derived probability is statistically meaningful. The resolution is set to be 22.5° × 10° (longitude by latitude) for most areas, 30° × 25° poleward of 65°S latitude, and 30° × 17.5° poleward of 55°N latitude. The coarse resolutions in the polar regions help to compensate for the sparse data coverage there. The resolution in the east-west direction is more relaxed than in the north-south direction, consistent with the observation in Figure 7a that the probability distribution tends to be more east-west stretched. The IUVS estimate of the auroral probability, shown in Figure 8b given by the number of detections divided by a total number of observations within each bin. For a side-by-side comparison, we transfer our estimate as given in Figure 7a to the coarse grid by applying Equation 3 and show the results in Figure 8c.

As seen in Figure 8, the model and IUVS data show generally consistent spatial distributions of the discrete auroral occurrence probability. Both are in overall close agreement, especially revealing a greatly increased chance of auroral observations over small-scaled patches inside the region of strong crustal fields. The IUVS data show that the overall chances of auroral occurrence are 1.55% over strong field regions, 0.51% over weak field regions, and 0.78% globally. These numbers quantitatively agree with our numerical prediction in Figure 7a during normal solar activities. The model-data discrepancy, on the other hand, may be explained by the fact that the data were collected under a variety of conditions while our simulations are under a limited number of boundary conditions. For example, the slightly higher auroral occurrence probability in the northern weak crustal field regions from the IUVS data perhaps reflects space weather effects, as suggested by the comparison of Figures 7a and 7b. Moreover, our model indicates a high probability near the north pole (particularly within 0°–60° longitudes). This is in part because the seasonal and IMF polarity dependence, which is not negligible as illustrated by our case comparisons in the SI, is only simply accounted for by assigning each case with equal weight. Furthermore, it is still unknown how the probability distribution is affected when the crustal field has a different orientation during intermediate seasons between equinoxes and solstices, or when the IMF direction deviates from the Parker spiral approximation, or when the IMF is also time-varying (e.g., at sector boundary crossings). All of these factors complicate the interpretation of the discrepancy between the model and data. Although the ICME case has naturally included these complexities, they are mixed together and difficult to disentangle.

4. Discussion

4.1. Local Magnetic Field Direction

We have shown that the crustal magnetic field strength is an important parameter in regulating the occurrence probability distribution of discrete aurora. It is empirically found that the surface area is roughly divided into strong and weak crustal field regions using the threshold strength of 50 nT at 150 km altitude. Such a division is most prominent in distinguishing between open and closed magnetic field topologies (Figures 3 and 6) and is also effective in differentiating the degree of the open magnetic field convergence (Figure 4), both of which work to determine where auroral electron precipitation may take place and produce detectable emissions. The next question to ask is, how about the magnetic field direction? Safaeinili et al. (2007) reported a significant correlation between intensified total electron contents derived from MEX measurements and vertical crustal

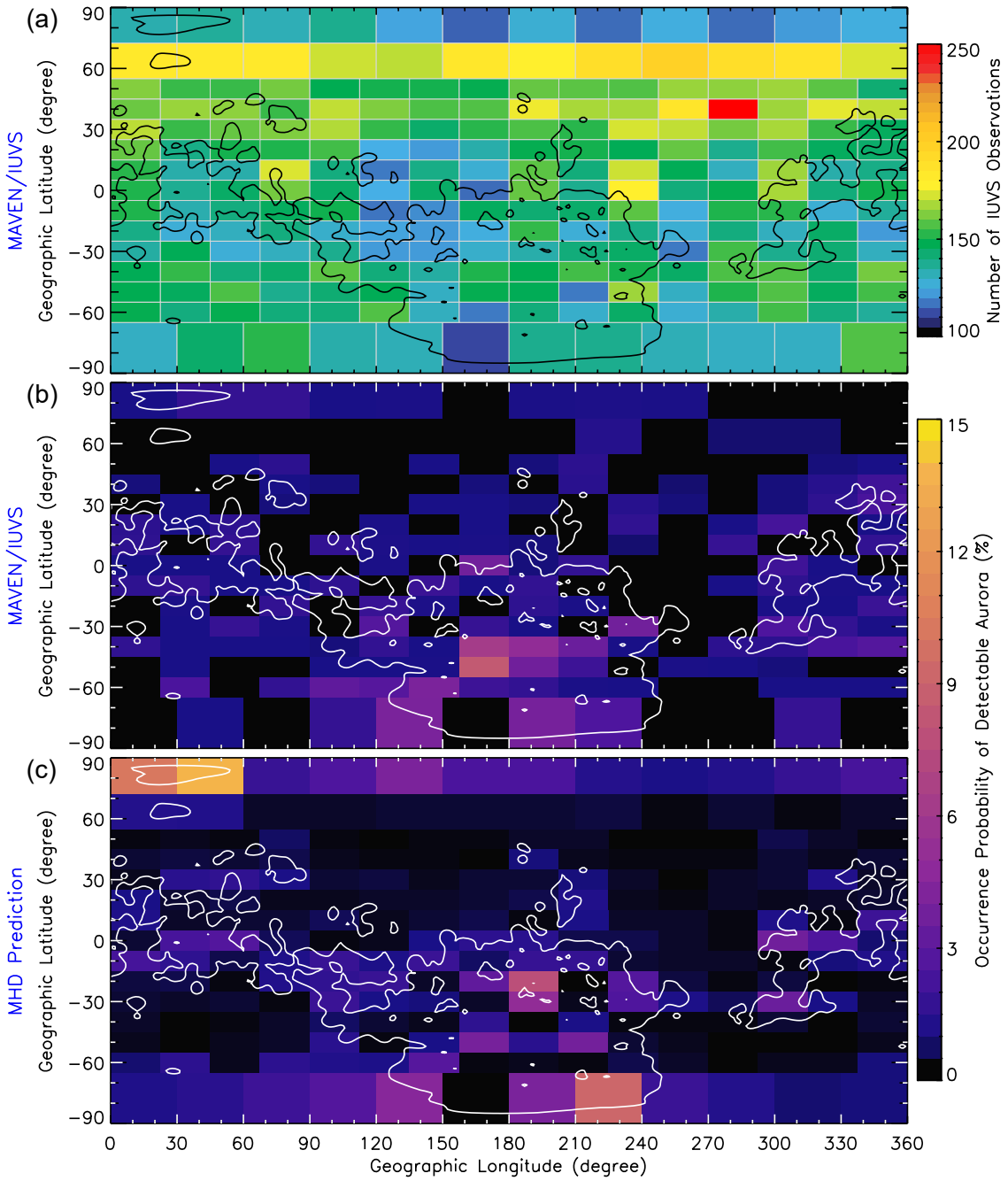

Figure 8. (a) Longitude-latitude distribution of the number of Mars Atmosphere and Volatile EvolutioN Imaging UltraViolet Spectrograph (IUVS) nightside discrete auroral observations (including detections and non-detections). An ad-hoc irregular grid is used, which is coarser near the north and south polar regions. (b)–(c) Auroral occurrence probability averaged within the longitude-latitude bins, from IUVS data and from our magnetohydrodynamic prediction (Figure 7a), respectively.

field directions. Although auroral events often occurred where the crustal field line was close to vertical, it was noticed by Gérard et al. (2015) that many times aurora was not observed during the MEX passage of vertical field regions and sometimes the crustal magnetic field near auroral sites was even horizontally oriented. These seemingly conflicting findings necessitate the investigation of the role of the magnetic field direction in auroral occurrence, which is still uncertain.

Figure 9 examines the probability of magnetic field lines being nearly vertical or horizontal on the nightside at 150 km altitude, during quiet solar activity and the 2017 ICME event. The magnetic field includes both the

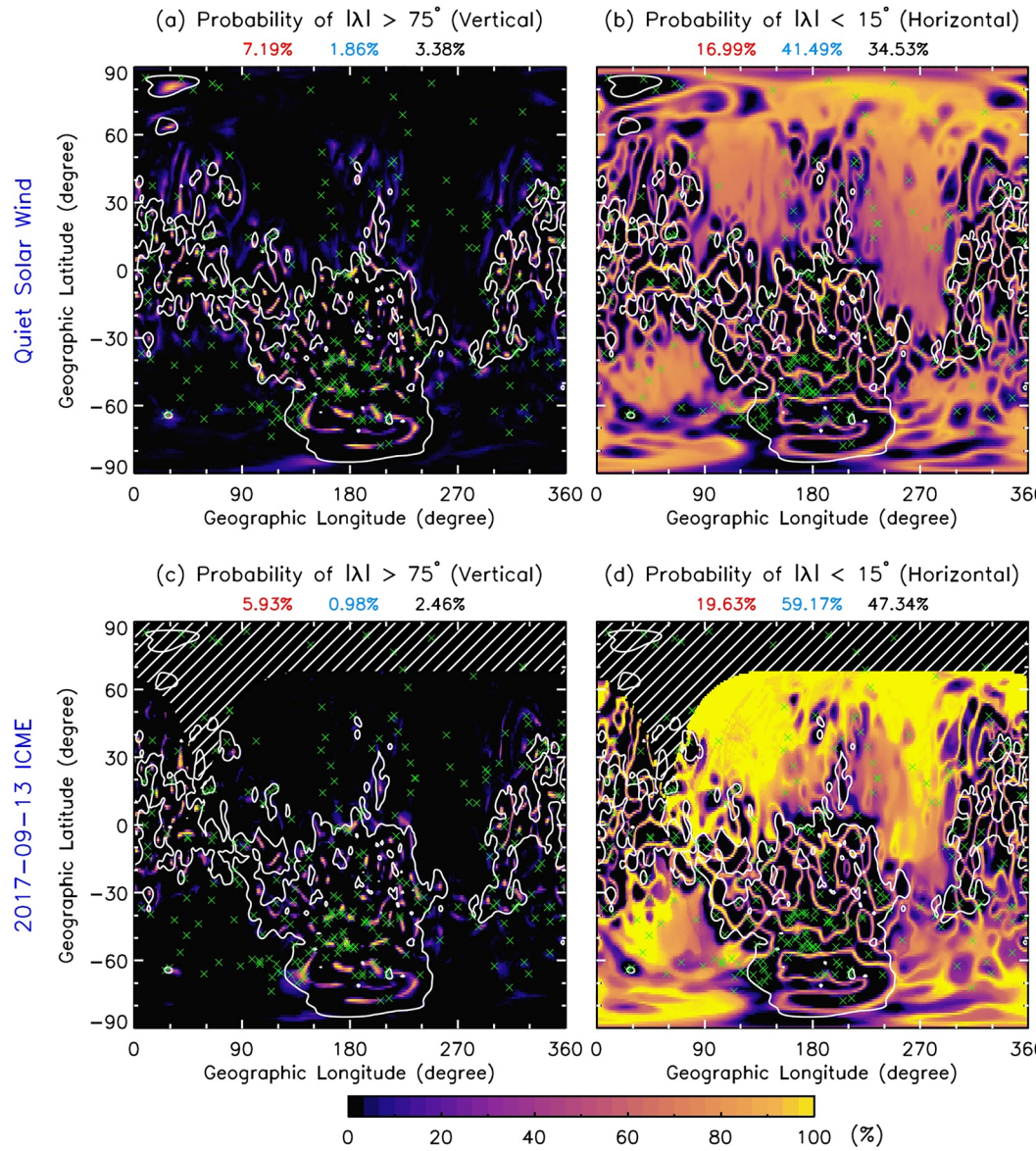

Figure 9. Magnetohydrodynamic-derived probability of magnetic field lines being (left) nearly vertical or (right) nearly horizontal at 150 km altitude on the nightside, which is defined to have an absolute dip angle with respect to the horizontal plane greater than 75° or less than 15°, respectively. The magnetic field includes both the intrinsic crustal field and induced field components. The top row shows the results that are arithmetically averaged among the eight quiet-solar-wind cases, and the bottom row is for the 13 September 2017 interplanetary coronal mass ejection event. The overall chances over strong and weak crustal field regions as well as globally are calculated and marked on top of the panels in red, blue, and black, respectively. Green '×' symbols mark the auroral occurrence sites inferred from Mars Atmosphere and Volatile EvolutioN Imaging UltraViolet Spectrograph limb scans above 100 km altitude.

crustal and induced field components, self-consistently calculated over the course of planetary rotation. The dip angle of the magnetic field, λ, is measured from the horizontal plane and is defined to be positive (negative) if the field has a radially outward (inward) component. For reference, we include in the SI (Figure S9, panel (a)) the distribution of the intrinsic crustal field dip angle, which shows that vertically oriented crustal magnetic fields spread throughout the globe and rapidly switch between outward and inward directions. After the induced field is considered, however, the MHD magnetic field over weak crustal field regions is on average more horizontal than vertical and the degree of horizontal orientation is further enhanced during the ICME event. In contrast, the field direction (and also the radial component of the magnetic field) over strong crustal field regions are less impacted, although fine structures are smeared out to some extent by the induced field. See the SI (Figures S9-S17) for a

detailed examination of the longitude-latitude distributions of the magnetic field dip angle and radial component in all the quiet-solar-wind cases and the ICME case. As a result, as illustrated by Figure 9, nearly vertical ($|\lambda| > 75°$) and nearly horizontal ($|\lambda| < 15°$) field lines are more likely present inside strong and weak crustal field regions, respectively. Although this trend of the magnetic field direction appears to be consistent in a rough sense with that of the auroral occurrence probability, there are findings as listed below for us to reject the magnetic field direction as a determining factor.

First, Figures 9a and 9c show that no aurora was observed by IUVS over many areas inside strong crustal field regions where the magnetic field direction is almost always vertical. In contrast, disproportionately more auroral events were observed by IUVS over weak crustal field regions in the northern hemisphere, even though the magnetic field over there has a very high chance to be horizontal (particularly during the ICME). Second, the overall chances of having the nearly-vertical magnetic field direction are ~four times greater than those from IUVS auroral observations, when comparing the values of 7.19%, 1.86%, and 3.38% (see Figure 9a) against 1.55%, 0.51%, and 0.78% (as discussed in Section 3.2) over strong and weak crustal field regions and across the globe, respectively. Third, and more importantly, our study suggests that solar activity would result in a decrease in the probability of vertically oriented magnetic field lines, which is opposite to the trend of increasing auroral occurrence during space weather events. Altogether, we conclude that the magnetic field direction itself is not determinative for the occurrence of aurora. It should be pointed out that it is not in conflict with the IUVS observation by Schneider et al. (2021) that there tend to be more auroral events where the radial component of the crustal field is stronger. The correlation with the vertical orientation of the magnetic field or the strength of its radial component reflects the high probability of auroral occurrence in strong crustal field regions but does not constitute a causal relationship.

4.2. Discrete Auroral Sources

The self-consistent simulation of the plasma and magnetic field in the MHD model provides us with a unique means to investigate where auroral electrons originate. Figure 10 shows example open magnetic field lines (blue) that connect the nightside ionosphere in the strong crustal field regions (white dots) and 5000 km altitude (red dots), in a quiet-solar-wind case ($L_s = 0°$, IMF $B_Y < 0$) at a specific time point when the strongest crustal field region is located near dawn. This represents the same situation as in Figures 2d–2f. In our discussions in Section 3, we consider that MHD thermal electrons in the high-energy tail at the red dots precipitate along the open field lines and excite the atmosphere at the white dot positions, but have not yet discussed where these precipitating populations originate. To figure that out, we use the MHD-calculated velocity field to trace the streamlines backward from the red dots until either 100 km altitude or the spherical surface of $r = 5\ R_M$ is reached. As shown in Figure 10, the extracted streamlines are indicated in yellow, whose starting positions are highlighted by green dots. For those streamlines originating in the far upstream, we only show their portion downstream of 5,000 km altitude for clarity. For reference, we derive and superpose in the figure the 3-D snapshots of the bow shock (BS) and induced magnetospheric boundary (IMB), using the algorithm described in detail by Fang et al. (2015).

It is seen in Figure 10 that, auroral precipitation within a certain geographic area may come from different places in the magnetosphere. In this specific case for auroral occurrence in the nightside ionosphere at dawn, the vast majority of electron precipitation at high altitudes is activated in the magnetotail on the dawn side and very few occur near the inner edge of the magnetosheath on the dusk side. The streamlines passing through these precipitation source regions illustrate the flow of plasma and help us to identify their origins. Our model results disagree with the prevailing hypothesis that discrete aurora results from the direct entry of magnetosheath plasma over a cusp-like structure. Instead, most of the plasma in the precipitation source region (76% in this example) originates in the upstream solar wind, with the rest originating in the ionosphere (see the green dots at low altitudes particularly in Figure 10d). As readily seen in Figures 10a and 10b, those solar wind electrons pass through the sheath region into the dayside magnetosphere and then convect toward the magnetotail. Particle precipitation is triggered in the tail where a magnetic connection with the ionosphere is formed. From the MHD perspective, there are no cusp-like open magnetic flux tubes to allow the direct entry of the shocked solar wind plasma inside the nightside magnetosheath. In contrast, discrete aurora at Mars is associated with the recycling of magnetospheric electrons in the tail, which is somehow analogous to terrestrial regular auroral process. This study suggests that some nightside magnetospheric electrons, rather than moving tailward, are able to return to the planet when ambient magnetic field lines are open and connected to the ionosphere. When the resulting electron precipitation is strong

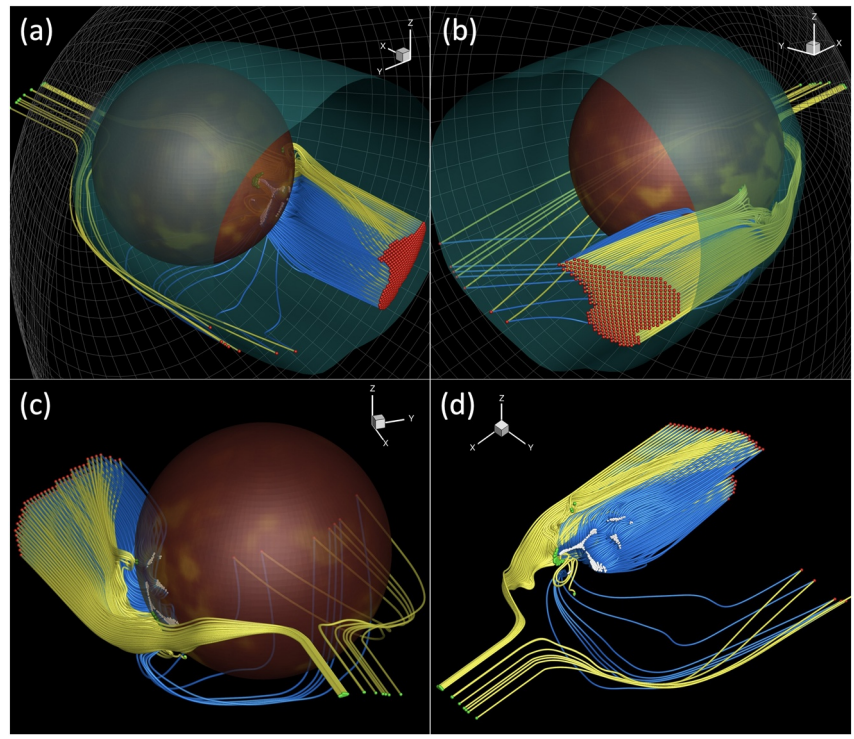

Figure 10. Open magnetic field lines (in blue) that are connected between the nightside ionosphere within 120°–180° longitudes and 30°S − 70°S latitudes at 150 km altitude (white dots) and 5,000 km altitude (red dots). The plasma flow streamlines that pass through the red dots are indicated by yellow lines, whose starting positions are marked by green dots. While a small fraction of the streamlines originates in the ionosphere, most of them originate in the upstream solar wind, cross the BS (gray grid) and induced magnetospheric boundary (cyan surface), and flow within the magnetosphere. These results are obtained in the quiet solar wind magnetohydrodynamic case of $L_s = 0°$, interplanetary magnetic field $B_Y < 0$, at the time when the subsolar longitude is 271.7° (see Figures 2d–2f). All of the panels show the same results except different looking directions, as indicated by the orientation of the Mars centred Solar Orbit *X-Y-Z* axes in the panel corners.

enough to cause ample atmospheric excitation, auroral emissions are detectable. Our model shows a tailward extension of open field lines in the tail, which is consistent with MAVEN-derived magnetic field topology distributions (Xu et al., 2020). As nearly all of the nightside-connected open field lines are confined well within the central magnetotail (SZA > 135°) far away from Mars (see Figure 2), our findings disagree with the hypothesis that discrete aurora is mainly produced from direct penetration of magnetosheath plasma.

4.3. Model Limitation

Under MHD fluid-like approximations, kinetic effects are not accounted for in this work. For example, we consider high-energy-tail electron populations from MHD plasma solutions under a Maxwellian approximation and neglect the effects due to non-thermal plasma distributions in the Mars weak magnetic field environment (e.g., Fang, Liemohn, et al., 2008). The hot electrons consist of shocked solar wind plasma and perhaps energized photoelectrons that make their way into the Martian wake. A local particle-in-cell calculation recently by Poppe et al. (2021) suggests that differential penetration of magnetospheric electrons and ions leads to the formation of quasi-static, field-aligned potentials. The resulting upward-pointing electric field exerts a downward acceleration on precipitating electrons, which is greater in a stronger ambient crustal field. This may explain the MEX observation of precipitating auroral electrons with an energy flux occasionally as high as 10 erg/cm^2/s (Gérard et al., 2015).

On the other hand, the magnetic mirroring effect, which reflects back incident particles in a converging magnetic field geometry (e.g., Lillis & Fang, 2015), is neglected in our calculations. The conservation of the first adiabatic invariant in the absence of field-aligned potentials results in the existence of a loss cone in particle pitch angle distributions. Electrons outside of the loss cone are magnetically reflected such that only those within the loss

cone are able to reach low altitudes and excite the atmosphere. As a result, particle precipitation as given by Equations 1 and 2 may need a correction factor of $\sin^2(\alpha_{LC})$ to take into the magnetic mirroring effect, where α_{LC} is the opening angle of the bounce loss cone. We have

$$\sin^2(\alpha_{LC}) = \frac{B_1}{B_2}\left(1 + \frac{e\Delta V}{E}\right), \tag{4}$$

where B_1 and B_2 stand for the magnetic field strengths in high-altitude source regions (i.e., at 5,000 km in this work) and in the upper atmosphere, respectively. E is the initial energy of precipitating electrons and ΔV stands for the parallel electric potential drop. In the absence of the field-aligned potential drop, $\sin^2(\alpha_{LC})$ is reduced to $\frac{B_1}{B_2}$.

We examine the ratio of $\frac{B_1}{B_2}$ along open field lines for discrete aurora in a specific quiet solar wind case of $L_s = 0°$, IMF $B_Y < 0$. As illustrated in Figure S18 and discussed in the SI, the ratio is smaller, or magnetic mirroring is larger, by a factor ranging from ~3 to ~8 in the region of strong crustal fields than in the region of weak crustal fields, depending on the planetary orientation to the Sun. When the strongest crustal field region faces the Sun and moves onto the nightside, the $\frac{B_1}{B_2}$ contrast for the nightside aurora between strong and weak crustal field regions is minimum and maximum, respectively. This highlights the importance of the induced magnetic field resulting from the solar wind-Mars interaction, which is notably enhanced on the dayside than on the nightside. According to the estimation by Poppe et al. (2021), the field-aligned potential drop inside strong crustal field regions is significantly higher than that inside weak crustal field regions, by a factor of ~4. In addition, it is worth noting that an enhanced potential drop not only results in more electron acceleration and thus an increase in precipitating electron energy fluxes, but also effectively weakens the magnetic mirroring effect by increasing the loss cone angle (see Equation 4). Moreover, we note that both of the effects become less important over weak crustal field regions. Altogether, it is implied that the consequences of magnetic mirroring and field-aligned potentials, which are opposite in their effects on precipitating energy fluxes, compensate to a comparable extent for each other. Although these two effects are currently neglected due to the limitation of our model, their combined effects actually have been greatly reduced in comparison with their individual effects. Conversely, considering one of the effects but not the other would lead to greater errors. Given the great challenge in globally and self-consistently modeling these two effects at the same time, we neglect them altogether in this work.

It should be stressed that our numerical method achieves a reasonably good agreement between the predicted auroral occurrence probability and MAVEN and MEX satellite observations, albeit neglecting this particle acceleration and angular scattering processes. This in turn suggests that the field line topology and magnetic field convergence play a critical role in determining the auroral morphology (i.e., where a detectable auroral event may happen), which is the focus of this study. Field-aligned potentials and magnetic mirroring effects, on the other hand, may be important in shaping precipitating particle energy fluxes and therefore auroral brightness but are likely not critical factors in auroral morphology. In addition, planetary ions may be accelerated and directed by electromagnetic fields back to the planet and bombard the upper atmosphere (e.g., Fang et al., 2013; Wang et al., 2015). How the atmospheric excitation by precipitating planetary ions compares with or contaminates that of discrete electron aurora is unknown and is subject to future study.

5. Summary and Conclusions

This paper represents the first attempt to theoretically predict the occurrence location and probability of discrete electron aurora at Mars on a planetary scale. Discrete aurora manifests itself as a patchy and sporadic phenomenon. Its seemingly stochastic behavior poses a daunting challenge for understanding how and where auroral electron precipitation takes place in the ionosphere. To address this challenge, we apply the state-of-the-art global MHD model to characterize the near-Mars plasma and magnetic field environments, whose spatial and temporal dynamics are self-consistently described by solving the ionosphere and magnetosphere and their interaction with the impinging solar wind and IMF from a system perspective. The model-calculated magnetic field consists of the intrinsic crustal field and the induced field. We run the MHD model in a time-dependent manner over the planetary rotation period and examine the system dynamics under quiet and disturbed space weather conditions. The former is realized by statistically averaging eight solar minimum quiet-solar-wind cases (four equinox/solstice seasons by two IMF polarities). The latter is through the study of the system responses to the 13 September 2017 ICME event.

In this work, we consider two critical prerequisites for the occurrence of detectable discrete electron aurora in the nightside ionosphere. First, electron precipitation at high altitudes is triggered by the presence of open magnetic field lines that have footpoints in the ionosphere. Open magnetic field lines establish a direct magnetic connection between precipitation source regions (at 5,000 km altitude in this work) and destination regions. Within the limitation of the MHD fluid-like approximation, we focus on electrons in the high energy tail (>30 eV) of Maxwellian energy distribution, below which incident particles are absorbed by the exosphere and cannot reach auroral altitudes. Second, to generate an auroral event detectable by current technology, precipitating electrons must carry sufficient energy fluxes to produce ample auroral emissions. Consistent with MEX observations, we assume a threshold energy flux of 0.1 erg/cm^2/s in our calculations. For a longitude-latitude position in the nightside ionosphere, the auroral occurrence is thus subject to the combined probabilities of the above two scenarios. The main findings of this study are summarized as follows.

1. Magnetic field topology on the nightside, especially below ~800 km altitude, is highly correlated with the crustal magnetic field strength. Using the empirically-derived, threshold crustal field magnitude of 50 nT at 150 km altitude, we can roughly divide the surface area into strong and weak crustal field regions, which occupy approximately 28% and 72% of the global area, respectively. Our results show that magnetic field lines over strong crustal field regions are dominantly closed, except for embedded small-scale patches where magnetic field lines are more likely open. In contrast, weak crustal field regions are dominated by open/draped magnetic field topologies. Our model-derived probability distribution of magnetic field topology at 400 km altitude is in remarkably close agreement with that inferred from MGS data analysis.
2. The occurrence probability of detectable discrete electron aurora is concentrated on small-scale patches embedded inside strong crustal magnetic field regions during quiet solar activity. Over weak crustal field regions, the aurora may appear near the polar regions and also over a narrow latitude band west of the strongest crustal field area (roughly 0°–130° longitudes, 60°S–75°S latitudes). The overall chances of detecting aurora during quiet solar activity are 1.81%, 0.35%, and 0.77% over strong and weak crustal field regions and across the globe, respectively. In comparison, the corresponding overall chances derived from MAVEN IUVS limb scans are 1.55%, 0.51%, and 0.78%, respectively.
3. The higher probability of detecting a discrete auroral event over strong crustal field regions is attributed to the more pronounced magnetic field convergence there, which significantly intensifies the energy flux of precipitating electrons. The magnetic field focusing effect greatly compensates for the generally lower probability of open magnetic field topology, leading to a generally higher auroral occurrence probability.
4. The occurrence probability of discrete aurora is greatly enhanced during space weather events, particularly over weak crustal field regions. It is estimated that the overall chances of aurora occurrence during the extreme 13 September 2017 ICME event are 5.76%, 9.39%, and 8.30% over strong and weak crustal field regions and across the globe, respectively. These numbers indicate a moderate increase by a factor of three over strong crustal field regions and a dramatic increase by more than an order of magnitude over weak crustal field regions.
5. According to our prediction, discrete electron aurora occurs wherever the ionosphere is magnetically connected with the magnetosphere through open field lines. This implies a relatively high overall chance of ~20% for auroral occurrence on the nightside during quiet solar activity (see Figures 5a) and if there was a nearly perfect ultraviolet instrument flying above Mars. Due to the limitation of instrument sensitivities, however, the need for intense electron precipitation in practice drops the overall chance of detectable auroral occurrence to 0.77% across the globe. Although space weather events enhance the occurrence frequency, discrete aurora happens under quiescent solar conditions.
6. The comparison of our theoretical prediction with MAVEN and MEX data shows a reasonably good agreement. Most of the satellites observed discrete auroral events occurred where our model predicts a high probability of occurrence. The small discrepancies between the model and data are perhaps caused by either space weather effects, or our neglect of intermediate seasons (other than equinoxes and solstices), or the departure of the upstream IMF direction from our adopted Parker spiral approximation, or their combination.
7. Our model results do not support that the vertical magnetic field direction (as opposed to the open magnetic field topology) is a determining factor in the occurrence of discrete electron aurora. This conclusion is based on the lack of a strong correlation between the auroral occurrence location and the vertical field direction or the strength of the radial magnetic field component. Furthermore, they exhibit opposite responses to space weather events.

8. Our detailed examination of open magnetic field connection and plasma flow streamlines suggests that discrete electron aurora at Mars is unlikely caused by the direct entry of nightside magnetosheath plasma in a cusp-like process as speculated before. From the perspective of the MHD model, a discrete aurora is associated with the recycling of nightside magnetospheric electrons that have convected from the dayside magnetosphere, which is analogous to terrestrial regular auroral processes.

Data Availability Statement

The MHD simulation code is publicly available at https://clasp.engin.umich.edu/research/theory-computational-methods/swmf-downloadable-software/. The MAVEN IUVS data are publicly available at NASA Planetary Data System through https://pds-atmospheres.nmsu.edu/.

Acknowledgments
This work was supported by NASA Grant 80NSSC19K0562 and the NASA MAVEN project through the Mars Exploration Program. Resources supporting the MHD simulation were provided by the NASA High-End Computing Program through the NASA Advanced Supercomputing Division at Ames Research Center.

References

Acuna, M., Connerney, J., Wasilewski, P. a., Lin, R., Anderson, K., Carlson, C., et al. (1998). Magnetic field and plasma observations at Mars: Initial results of the mars global surveyor mission. *Science*, *279*(5357), 1676–1680.

Bertaux, J.-L., Leblanc, F., Witasse, O., Quemerais, E., Lilensten, J., Stern, S., et al. (2005). Discovery of an aurora on Mars. *Nature*, *435*(7043), 790–794. https://doi.org/10.1038/nature03603

Brain, D., Lillis, R., Mitchell, D., Halekas, J., & Lin, R. (2007). Electron pitch angle distributions as indicators of magnetic field topology near mars. *Journal of Geophysical Research: Space Physics*, *112*(A9), A09201. https://doi.org/10.1029/2007JA012435

Brain, D., Weber, T., Xu, S., Mitchell, D., Lillis, R., Halekas, J., et al. (2020). Variations in nightside magnetic field topology at mars. *Geophysical Research Letters*, *47*(19), e2020GL088921. https://doi.org/10.1029/2020GL088921

Deighan, J., Jain, S., Chaffin, M., Fang, X., Halekas, J. S., Clarke, J. T., et al. (2018). Discovery of a proton aurora at Mars. *Nature Astronomy*, *2*(10), 802–807. https://doi.org/10.1038/s41550-018-0538-5

Dubinin, E., Fraenz, M., Woch, J., Winnigham, J., Frahm, R., Lundin, R., & Barabash, S. (2008). Suprathermal electron fluxes on the nightside of mars: Aspera-3 observations. *Planetary and Space Science*, *56*(6), 846–851. https://doi.org/10.1016/j.pss.2007.12.010

Fang, X., Bougher, S. W., Johnson, R. E., Luhmann, J. G., Ma, Y., Wang, Y.-C., & Liemohn, M. W. (2013). The importance of pickup oxygen ion precipitation to the Mars upper atmosphere under extreme solar wind conditions. *Geophysical Research Letters*, *40*(10), 1922–1927. https://doi.org/10.1002/grl.50415

Fang, X., Liemohn, M. W., Nagy, A. F., Ma, Y., De Zeeuw, D. L., Kozyra, J. U., & Zurbuchen, T. H. (2008). Pickup oxygen ion velocity space and spatial distribution around mars. *Journal of Geophysical Research: Space Physics*, *113*(A2), A02210. https://doi.org/10.1029/2007JA012736

Fang, X., Ma, Y., Brain, D., Dong, Y., & Lillis, R. (2015). Control of Mars global atmospheric loss by the continuous rotation of the crustal magnetic field: A time-dependent MHD study. *Journal of Geophysical Research: Space Physics*, *120*(12), 10–926. https://doi.org/10.1002/2015JA021605

Fang, X., Ma, Y., Luhmann, J., Dong, Y., Brain, D., Hurley, D., et al. (2018). The morphology of the solar wind magnetic field draping on the dayside of mars and its variability. *Geophysical Research Letters*, *45*(8), 3356–3365. https://doi.org/10.1002/2018GL077230

Fang, X., Ma, Y., Masunaga, K., Dong, Y., Brain, D., Halekas, J., et al. (2017). The mars crustal magnetic field control of plasma boundary locations and atmospheric loss: Mhd prediction and comparison with maven. *Journal of Geophysical Research: Space Physics*, *122*(4), 4117–4137. https://doi.org/10.1002/2016JA023509

Fang, X., Randall, C. E., Lummerzheim, D., Solomon, S. C., Mills, M. J., Marsh, D. R., et al. (2008). Electron impact ionization: A new parameterization for 100 ev to 1 mev electrons. *Journal of Geophysical Research: Space Physics*, *113*(A9), A09311. https://doi.org/10.1029/2008JA013384

Gérard, J.-C., Soret, L., Libert, L., Lundin, R., Stiepen, A., Radioti, A., & Bertaux, J.-L. (2015). Concurrent observations of ultraviolet aurora and energetic electron precipitation with MARS express. *Journal of Geophysical Research: Space Physics*, *120*(8), 6749–6765. https://doi.org/10.1002/2015JA021150

Leblanc, F., Witasse, O., Lilensten, J., Frahm, R., Safaenili, A., Brain, D., et al. (2008). Observations of aurorae by spicam ultraviolet spectrograph on board mars express: Simultaneous aspera-3 and marsis measurements. *Journal of Geophysical Research: Space Physics*, *113*(A8), A08311. https://doi.org/10.1029/2008JA013033

Liemohn, M., Ma, Y., Nagy, A., Kozyra, J., Winningham, J., Frahm, R., et al. (2007). Numerical modeling of the magnetic topology near mars auroral observations. *Geophysical Research Letters*, *34*(24), L24202. https://doi.org/10.1029/2007GL031806

Lillis, R. J., & Brain, D. A. (2013). Nightside electron precipitation at mars: Geographic variability and dependence on solar wind conditions. *Journal of Geophysical Research: Space Physics*, *118*(6), 3546–3556. https://doi.org/10.1002/jgra.50171

Lillis, R. J., & Fang, X. (2015). Electron impact ionization in the martian atmosphere: Interplay between scattering and crustal magnetic field effects. *Journal of Geophysical Research: Planets*, *120*(7), 1332–1345. https://doi.org/10.1002/2015JE004841

Ma, Y., Fang, X., Halekas, J. S., Xu, S., Russell, C. T., Luhmann, J. G., et al. (2018). The impact and solar wind proxy of the 2017 september icme event at mars. *Geophysical Research Letters*, *45*(15), 7248–7256. https://doi.org/10.1029/2018GL077707

Ma, Y., Fang, X., Russell, C. T., Nagy, A. F., Toth, G., Luhmann, J. G., et al. (2014). Effects of crustal field rotation on the solar wind plasma interaction with mars. *Geophysical Research Letters*, *41*(19), 6563–6569. https://doi.org/10.1002/2014GL060785

Ma, Y., Russell, C., Fang, X., Dong, C., Nagy, A., Toth, G., et al. (2017). Variations of the martian plasma environment during the icme passage on 8 march 2015: A time-dependent mhd study. *Journal of Geophysical Research: Space Physics*, *122*(2), 1714–1730. https://doi.org/10.1002/2016JA023402

Ma, Y., Russell, C. T., Fang, X., Dong, Y., Nagy, A., Toth, G., et al. (2015). Mhd model results of solar wind interaction with mars and comparison with maven plasma observations. *Geophysical Research Letters*, *42*(21), 9113–9120. https://doi.org/10.1002/2015GL065218

Mitchell, D., Lin, R., Mazelle, C., Rème, H., Cloutier, P., Connerney, J., et al. (2001). Probing mars' crustal magnetic field and ionosphere with the mgs electron reflectometer. *Journal of Geophysical Research: Planets*, *106*(E10), 23419–23427. https://doi.org/10.1029/2000je001435

Morschhauser, A., Lesur, V., & Grott, M. (2014). A spherical harmonic model of the lithospheric magnetic field of mars. *Journal of Geophysical Research: Planets*, *119*(6), 1162–1188. https://doi.org/10.1002/2013JE004555

Poppe, A., Brain, D., Dong, Y., Xu, S., & Jarvinen, R. (2021). Particle-in-cell modeling of martian magnetic cusps and their role in enhancing nightside ionospheric ion escape. *Geophysical Research Letters*, *48*(1), e2020GL090763. https://doi.org/10.1029/2020GL090763

Safaeinili, A., Kofman, W., Mouginot, J., Gim, Y., Herique, A., Ivanov, A. B., et al. (2007). Estimation of the total electron content of the martian ionosphere using radar sounder surface echoes. *Geophysical Research Letters*, *34*(23), L23204 . https://doi.org/10.1029/2007GL032154

Schneider, N., Deighan, J. I., Jain, S. K., Stiepen, A., Stewart, A. I. F., Larson, D., et al. (2015). Discovery of diffuse aurora on mars. *Science*, *350*(6261), aad0313. https://doi.org/10.1126/science.aad0313

Schneider, N., Jain, S., Deighan, J., Nasr, C.-R., Brain, D., Larson, D., et al. (2018). Global aurora on mars during the september 2017 space weather event. *Geophysical Research Letters*, *45*(15), 7391–7398. https://doi.org/10.1029/2018GL077772

Schneider, N., Milby, Z., Jain, S., Gerard, J., Soret, L., Brain, D., & Deighan, J. (2021). Discrete aurora on MARS: Insights into their distribution and activity from MAVENS/IUVS observations. *JGR Space Physics*, *126*(10), e2021JA029428.

Schunk, R., & Nagy, A. (2009). *Ionospheres: Physics, plasma physics, and chemistry*. Cambridge University Press.

Smith, D. E., Zuber, M. T., Frey, H. V., Garvin, J. B., Head, J. W., Muhleman, D. O., et al. (2001). Mars orbiter laser altimeter: Experiment summary after the first year of global mapping of mars. *Journal of Geophysical Research: Planets*, *106*(E10), 23689–23722. https://doi.org/10.1029/2000JE001364

Soret, L., Gérard, J.-C., Libert, L., Shematovich, V. I., Bisikalo, D. V., Stiepen, A., & Bertaux, J.-L. (2016). Spicam observations and modeling of mars aurorae. *Icarus*, *264*, 398–406. https://doi.org/10.1016/j.icarus.2015.09.023

Verigin, M., Gringauz, K., Shutte, N., Haider, S., Szego, K., Kiraly, P., et al. (1991). On the possible source of the ionization in the nighttime martian ionosphere: 1. Phobos 2 harp electron spectrometer measurements. *Journal of Geophysical Research: Space Physics*, *96*(A11), 19307–19313. https://doi.org/10.1029/91JA00924

Wang, Y.-C., Luhmann, J. G., Fang, X., Leblanc, F., Johnson, R. E., Ma, Y., & Ip, W.-H. (2015). Statistical studies on mars atmospheric sputtering by precipitating pickup o+: Preparation for the maven mission. *Journal of Geophysical Research: Planets*, *120*(1), 34–50. https://doi.org/10.1002/2014JE004660

Winningham, J. D., Frahm, R. A., Sharber, J. R., Liemohn, M. W., Ma, Y., Coates, A. J., et al. (2005). Electron observations near martian aurora. *Eos Trans. AGU.*, *86*(52). Fall Meet. Suppl., Abstract SH42A-03. https://abstractsearch.agu.org/meetings/2005/FM/SH42A-03.html

Xu, S., Mitchell, D., Liemohn, M., Fang, X., Ma, Y., Luhmann, J., et al. (2017). Martian low-altitude magnetic topology deduced from maven/swea observations. *Journal of Geophysical Research: Space Physics*, *122*(2), 1831–1852. https://doi.org/10.1002/2016JA023467

Xu, S., Mitchell, D. L., Weber, T., Brain, D. A., Luhmann, J. G., Dong, C., et al. (2020). Characterizing mars's magnetotail topology with respect to the upstream interplanetary magnetic fields. *Journal of Geophysical Research: Space Physics*, *125*(3), e2019JA027755. https://doi.org/10.1029/2019JA027755

References From the Supporting Information

Gérard, J.-C., Soret, L., Libert, L., Lundin, R., Stiepen, A., Radioti, A., & Bertaux, J.-L. (2015). Concurrent observations of ultraviolet aurora and energetic electron precipitation with MARS express. *Journal of Geophysical Research: Space Physics*, *120*(8), 6749–6765. https://doi.org/10.1002/2015JA021150

Leblanc, F., Witasse, O., Lilensten, J., Frahm, R., Safaenili, A., Brain, D., & others (2008). Observations of aurorae by spicam ultraviolet spectrograph on board mars express: Simultaneous aspera-3 and marsis measurements. *Journal of Geophysical Research: Space Physics*, *113*(A8). https://doi.org/10.1029/2008JA013033

Ma, Y., Fang, X., Halekas, J. S., Xu, S., Russell, C. T., Luhmann, J. G., & others (2018). The impact and solar wind proxy of the 2017 september icme event at mars. *Geophysical Research Letters*, *45*(15), 7248–7256. https://doi.org/10.1029/2018GL077707

Morschhauser, A., Lesur, V., & Grott, M. (2018). A spherical harmonic model of the lithospheric magnetic field of mars. *Journal of Geophysical Research: Planets*, *119*(6), 1162–1188. https://doi.org/10.1002/2013JE004555

Smith, D. E., Zuber, M. T., Frey, H. V., Garvin, J. B., Head, J. W., Muhleman, D. O., & others (2001). Mars orbiter laser altimeter: Experiment summary after the first year of global mapping of mars. *Journal of Geophysical Research: Planets*, *106*(E10), 23689–23722. https://doi.org/10.1029/2000JE001364